Medical Image Analysis 88 (2023) 102831

Contents lists available at ScienceDirect

Medical Image Analysis

journal homepage: www.elsevier.com/locate/media

Cerebrovascular super-resolution 4D Flow MRI – Sequential combination of resolution enhancement by deep learning and physics-informed image processing to non-invasively quantify intracranial velocity, flow, and relative pressure

E. Ferdian [a,1,*], D. Marlevi [b,1], J. Schollenberger [c], M. Aristova [d], E.R. Edelman [b], S. Schnell [d,e], C.A. Figueroa [c], D.A. Nordsletten [c,f,2], A.A. Young [a,f,2]

[a] University of Auckland, Auckland 1142 New Zealand
[b] Massachusetts Institute of Technology, Cambridge, MA 02139 USA
[c] University of Michigan, Ann Arbor, MI 48109, USA
[d] Northwestern University, Chicago, IL 60611, USA
[e] University of Greifswald, Greifswald 17489, Germany
[f] King's College London, London, SE1 7EH, UK.

ARTICLE INFO

Keywords:
Super-resolution 4D flow MRI
Deep learning
Relative pressure
Cerebrovasculature

ABSTRACT

The development of cerebrovascular disease is tightly coupled to regional changes in intracranial flow and relative pressure. Image-based assessment using phase contrast magnetic resonance imaging has particular promise for non-invasive full-field mapping of cerebrovascular hemodynamics. However, estimations are complicated by the narrow and tortuous intracranial vasculature, with accurate image-based quantification directly dependent on sufficient spatial resolution. Further, extended scan times are required for high-resolution acquisitions, and most clinical acquisitions are performed at comparably low resolution (>1 mm) where biases have been observed with regard to the quantification of both flow and relative pressure. The aim of our study was to develop an approach for *quantitative intracranial super-resolution 4D Flow MRI*, with effective resolution enhancement achieved by a dedicated deep residual network, and with accurate quantification of functional relative pressures achieved by subsequent physics-informed image processing. To achieve this, our two-step approach was trained and validated in a patient-specific *in-silico* cohort, showing good accuracy in estimating velocity (relative error: 15.0 ± 0.1%, mean absolute error (MAE): 0.07 ± 0.06 m/s, and cosine similarity: 0.99 ± 0.06 at peak velocity) and flow (relative error: 6.6 ± 4.7%, root mean square error (RMSE): 0.56 mL/s at peak flow), and with the coupled physics-informed image analysis allowing for maintained recovery of functional relative pressure throughout the circle of Willis (relative error: 11.0 ± 7.3%, RMSE: 0.3 ± 0.2 mmHg). Furthermore, the quantitative super-resolution approach is applied to an *in-vivo* volunteer cohort, effectively generating intracranial flow images at <0.5 mm resolution and showing reduced low-resolution bias in relative pressure estimation. Our work thus presents a promising two-step approach to non-invasively quantify cerebrovascular hemodynamics, being applicable to dedicated clinical cohorts in the future.

1. Introduction

Changes in regional hemodynamics are intimately coupled to the manifestation of cerebrovascular disease, making the quantification of flow and pressure key to improved individualized risk stratification. Variations in pressure throughout the cerebrovasculature have been particularly highlighted in a number of clinical scenarios: the functional impact of intracranial atherosclerosis linked to regional changes in intravascular pressure (Leng et al., 2014), the likelihood of cerebral aneurysm growth coupled to regional pressure gradients (Penn et al.,

* Corresponding author.
[1] First authorship is shared between E.F. and D.M., with both authors contributing equally to the work.
[2] Last authorship is shared between D.A.N and A.A.Y., with both authors contributing equally to the work.

https://doi.org/10.1016/j.media.2023.102831
Received 9 December 2021; Received in revised form 4 April 2023; Accepted 20 April 2023
Available online 22 April 2023

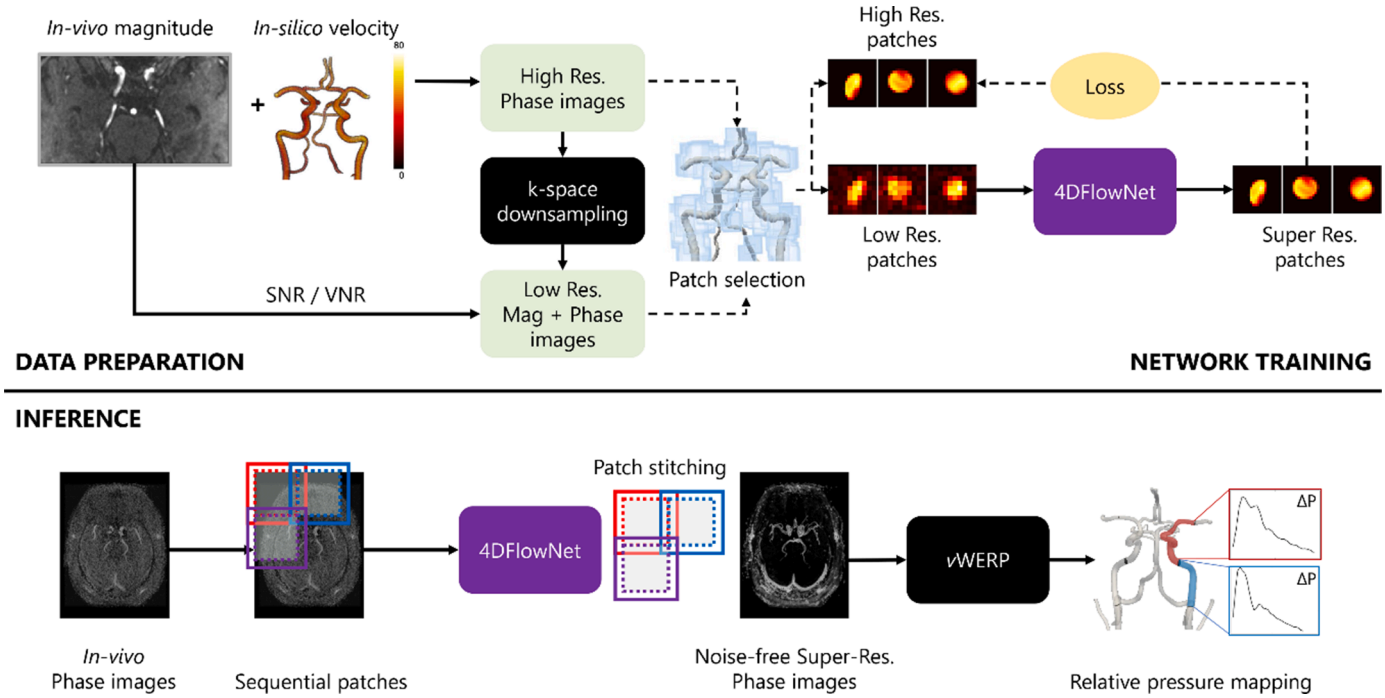

Fig. 1. Overview of the methodological framework including data preparation (top left), network training (top right), and inference (bottom) enabling super-resolved 4D Flow MRI with coupled quantification of hemodynamic relative pressures throughout the intracranial space.

2011), and experimental work showing altered pressure variations in arteriovenous malformations (Rivera-Rivera et al., 2018). While transcranial Doppler or 2D phase-contrast magnetic resonance imaging (PC-MRI) provide limited information on regional flow, it is through time-resolved three-dimensional phase-contrast magnetic resonance imaging (4D Flow MRI) that full-field hemodynamic mapping can be achieved (Stankovic et al., 2014). 4D Flow MRI has been used in a number of studies to capture cerebrovascular flow phenomena (Morgan et al., 2021), and in combination with physics-informed image processing, quantification of relative pressure is permitted (Marlevi et al., 2021b). However, the spatial resolution has shown to be critically important for the accurate image-based quantification of both cerebrovascular flow (Aristova et al., 2019) and relative pressure (Marlevi et al., 2021b). Specifically, in standard clinical systems settings for cerebrovascular 4D Flow MRI of around dx = 1 mm, significant biases have been indicated when quantifying flow and relative pressure through the circle of Willis (Aristova et al., 2019; Marlevi et al., 2021b). While imaging can be theoretically performed at finer spatial sampling (sub-mm resolution), more averages would be required to compensate for increased image noise, which would ultimately result in clinically infeasible scan times. There thus remains a need for effective approaches to achieve high-resolution flow imaging in order to allow for accurate quantification of cerebrovascular hemodynamics in a clinical setting.

To address the need for improved spatial resolution, high-Tesla approaches have been proposed (Gottwald et al., 2020; Metcalf et al., 2010), however, are inherently limited to specialized imaging systems. The use of image-guided computational fluid dynamics (CFD) modeling has also been explored (Perez-Raya et al., 2020; Schollenberger et al., 2021), however, generally put high demand on available computational resources, and further depend on boundary conditions typically requiring additional specialized imaging protocols (Schollenberger et al., 2021).

As an alternative to these deterministic approaches, deep learning methods have recently been applied in the field of medical image enhancement. For MRI, deep learning methods have been proven to enable data denoising (Rutkowski et al., 2021), artefact compensation (Oksuz et al., 2018), and to generate super-resolution anatomical reconstructions of the brain (Plenge et al., 2012). For flow-based MRI, 2D-studies have shown the ability to generate accelerated reconstructions of phase-contrast images (Nath et al., 2020), as well as enable automatic flow quantification over network-segmented flow domains (Bratt et al., 2019). For 4D Flow MRI, Ferdian et al. (Ferdian et al., 2020) proposed the so-called 4DFlowNet to generate super-resolution 4D Flow MRI data from low-resolution input, with the network trained on synthetic pairs of low/high-resolution images generated from aortic CFD simulations. Other alternatives include Rutkowski et al. (Rutkowski et al., 2021) using a convolutional neural network (CNN) generating denoised 4D Flow images, and Fathi et al. (Fathi et al., 2020) using a Physics-Informed Neural Network (PINN) to generate super-resolution 4D Flow images, with ground-truth CFD data used for network testing. Whilst 4DFlowNet was only tested on large-vessel aortic flows, both the CNN and the PINN-based alternatives were implemented on either phantom-data resembling cerebrovascular flow, or on selected *in-vivo* sets. However, no extended quantitative analysis has been performed for *in-vivo* usage in a cerebrovascular setting. Furthermore, neither of the above-mentioned networks (2D or 3D) have been tested with respect to functional pressure measurements, and it remains unknown whether pressure changes through the image domain are maintained or even improved by applying any of these super-resolution procedures.

The purpose of this study is therefore to develop an approach for *quantitative intracranial super-resolution 4D Flow MRI*, specifically evaluating whether a *combination* of dedicated deep learning and subsequent higher-dimensional image processing could allow for accurate and comprehensive estimation of velocity, flow, and relative pressure throughout the cerebrovasculature. Specifically, our study aims include (1) assessing whether a dedicated cerebrovascular super-resolution network could improve estimates of regional intracranial velocities and flows, and (2) evaluating whether the two-step combination of deep learning based super-resolved images and sequential physics-informed image processing would allow for accurate recovery of *functional* relative pressures throughout the cerebrovascular space. To achieve this, the existing super-resolution network 4DFlowNet (Ferdian et al., 2020) and the physics-informed virtual work-energy relative pressure approach

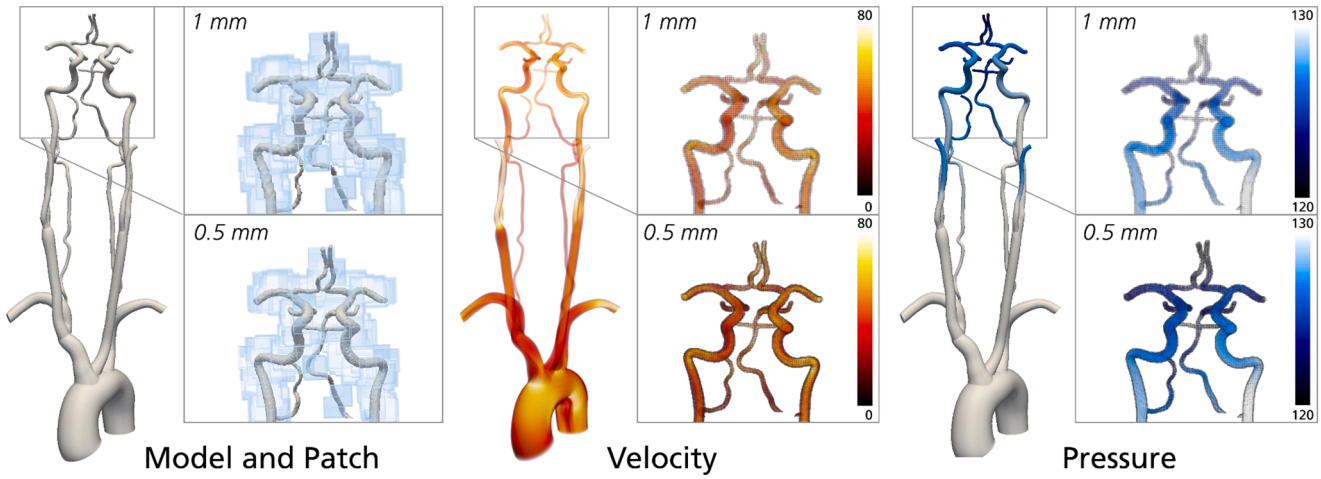

Fig. 2. Overview of the in-silico input used for re-training of the 4DFlowNet network, showing one of the four used models (Subject 3b). From left to right: model overview and patch generation through the proximal cerebrovascular ROI; velocity field (color range 0 - 80 cm/s); pressure field (color range 120–130 mmHg). Note that examples are shown for the low/high-resolution pair of 1.0/0.5 mm isotropic.

*v*WERP (Marlevi et al., 2019) are for the first time utilized in sequence, and applied in a cerebrovascular imaging setting, with dedicated patient-specific CFD models and clinically acquired 4D Flow MRI used to train, test, and validate the recovery of comprehensive intracranial hemodynamics. Once validated against ground truth reference, and once compared against alternative deterministic super-resolution methods, our two-step approach is also applied to an *in-vivo* cohort of subjects scanned at multiple resolutions, demonstrating the potential of super-resolution imaging in a clinical setting. To summarize, the main contributions of this paper thus lie in the ability for quantitative intracranial flow imaging, using a two-step approach of deep learning-enhanced 4D Flow MRI and subsequent physics-informed image processing to jointly overcome estimation biases otherwise observed in clinical level input data.

2. Methods

This section is structured as follows: first, a methodological overview of the deep learning framework for super-resolution 4D Flow MRI is provided (Section 2.1), including specifications of network architecture (Section 2.1.1) and loss function (Section 2.1.2). Second, details of the utilized training and testing data are provided (Section 2.2), including patient-specific *in-silico* models (Section 2.2.1), acquired *in-vivo* data (Section 2.2.2), and the assembly of both into patches for dedicated training (Section 2.2.3). Lastly, details of performance quantifications are provided (Section 2.3), including *in-silico* validation (Section 2.3.1) and clinical *in-vivo* implementation (Section 2.3.2). Additionally, Fig. 1 presents an illustrative overview of the methodological basis of the paper.

2.1. Deep learning framework

2.1.1. Network architecture

To achieve super-resolution flow images, we utilize the deep residual network structure of 4DFlowNet (Ferdian et al., 2020); a previously published network validated for large-vessel aortic flows. Briefly, the architecture is based on a central upsampling layer (using bilinear interpolation) surrounded by a series of stacked residual blocks (RB), with preceding RBs denoising and pre-processing the input, and subsequent RBs refining and sharpening the predicted output. During inference, both low-resolution magnitude and velocity phase 3D image patches were utilized as input, with super-resolution 3D velocity patches generated as output; all as described in previous work (Ferdian et al., 2020) (an overview of the network architecture is provided in Appendix A and coupled Appendix Fig. A.1).

We used a similar design to the original 4DFlowNet architecture (Ferdian et al., 2020), with adjustments introduced for its application on cerebrovascular flow data:

1 Patch input size was changed from an original 16-voxel cube, to a 12-voxel cube, accounting for the smaller vessel sizes encountered in the cerebrovascular space. The new patch size was empirically determined during preliminary testing, with a 12-voxel cube deemed optimal in the trade-off between including excessive amounts of non-flow regions (using a large patch size), and excluding too much flow information (using a small patch size).
2 The original hyperbolic tangent activation functions at the output layers were removed, resulting in linear output layers. This was introduced to allow for unbounded output values. While in our work, the output values were still bounded between [−1, 1] by the normalized data and the loss function definition (see below), a linear output layer would allow for the possibility of automatic velocity aliasing (phase-wrapped) correction in future work.
3 The gradient terms were removed from the loss function, following improvements observed in near-wall velocity estimates in the preliminary data assessment.

The modified network was trained using an Adam optimizer, with a learning rate empirically set to $2 \bullet 10^{-4}$. Batch sizes of 20 were used for training (based on the maximum number of batches allowed within our computational memory storage), and the model with the best validation loss was chosen. The model was trained for 60 epochs, whereafter no further improvements were observed. The network was implemented using Tensorflow 2.2.0 (Abadi et al., 2016), utilizing a Keras backend (training setup, hyperparameters, and trained weights are all publicly available at https://github.com/EdwardFerdian/4DFlowNet).

2.1.2. Loss function definition

For the loss function, the optimization target was set to minimize the mean squared error (MSE) between the generated super-resolution images, and the paired high-resolution input data. The voxel-wise loss was defined as the mean of the sum squared differences between Cartesian velocity components, (Δv_x^2, Δv_y^2 and Δv_z^2), given as

$$l_{MSE} = \frac{1}{N}\sum_{i=1}^{N} \Delta v_x^2 + \Delta v_y^2 + \Delta v_z^2 \quad (1)$$

where N is the total number of voxels in the assessed image domain

(patch). To compensate for imbalances between fluid and static tissue regions within a singular patch, the MSE was calculated separately for each region, respectively. To avoid network overfitting, an L2 regularization term was also included. The complete loss function was thus given as

$$loss = l_{MSE-vessel} + l_{MSE-non-vessel} + \lambda \sum_{i=1}^{N} w_i^2 \quad (2)$$

where $l_{MSE-vessel}$ and $l_{MSE-non-vessel}$ are the voxel-wise MSE loss in fluid and static tissue, respectively. λ is a coefficient regularizing the network weights w_i, assigned to $5 \cdot 10^{-7}$ after empirical evaluation of the overall loss vs. the network weights. Note that this differs from the original 4DFlowNet work (Ferdian et al., 2020), from which an additional velocity gradient loss was removed, and the L2 regularization added, respectively (all based on preliminary, empirical training and data evaluations).

2.2. Training and testing data

To train the super-resolution network, sets of low and high-resolution flow images needed to be collected. Whilst acquired, matched, integer pairs of clinical 4D Flow MRI data would represent a theoretically ideal training set, in practice it is very difficult to obtain such high-resolution, high-SNR, artifact-free *in-vivo* ground truth data suitable for training. Instead, we here propose a separate set of synthetic 4D Flow MRI originating from patient-specific cerebrovascular flow simulations. To improve clinical relevance, simulated data is combined with reference *in-vivo* scans by (1) transfer of realistic noise levels from *in-vivo* data to the simulated velocity sets, and (2) incorporation of relevant *in-vivo* magnitude images as complement to the simulated velocity sets (with reference magnitude images manually co-registered to the simulated sets); all to liken the utilized simulated training data to that of clinically acquired 4D Flow MRI datasets.

2.2.1. Patient-specific in-silico data

As a basis for training, anatomically accurate patient-specific CFD models of the arterial cerebrovasculature were used, providing both realistic velocity, flow, and reference pressure fields data (see Schollenberger et al. for complete model details (Schollenberger et al., 2021), and Fig. 2 for an illustrative model overview).

In short, models were created using a combination of patient-specific image sets, including T1-weighted MRI, time-of-flight (TOF) MRI, 2D phase contrast (PC) MRI, and MRI arterial spin labeling (ASL) (Schollenberger et al., 2020). Anatomical segmentations of the vasculature from the aortic root to the circle of Willis (CoW) were derived by combining T1-weighted MRI (mapping the aortic root to the carotid bifurcation) and TOF MRI (mapping the carotid bifurcation to the CoW). As inflow boundary condition, a pulsatile velocity profile derived from PC-MRI was prescribed at the inlet of the aortic root. Further, each outlet was coupled to a 3-element lumped parameter Windkessel model and calibrated using a combination of PC-MRI, non-selective ASL perfusion, and cuff pressure data (Schollenberger et al., 2021). 3D models were meshed using tetrahedral elements, with the incompressible Navier-Stokes equations solved iteratively using a stabilized finite-element formulation. Nodal velocity and pressure data was extracted after periodicity had been reached (≥4 cardiac cycles). The modeling and analysis were performed using the validated open-source framework CRIMSON (Arthurs et al., 2021). Model accuracy and patient-specific behavior were validated against vessel-specific ASL, with excellent agreement reported between modelled and measured cerebrovascular blood distributions. For a detailed description of model setup and validations, please see Schollenberger et al. (Schollenberger et al., 2021).

Data from four different image sets were generated:

- Subject 1 presenting without evidence of cerebrovascular disease, although exhibiting an incomplete CoW through right and left posterior communicating artery hyperplasia.
- Subject 2 presenting with severe stenosis in the right proximal internal carotid artery (ICA, 70–99% based on velocity criteria from duplex ultrasound) and a complete CoW.
- Subject 3a presenting with a bilateral carotid stenosis (80–90% in the right proximal ICA, and 60% in the left proximal ICA, based on CTA image criteria), and a CoW exhibiting right P1 segment and distal right vertebral artery hypoplasia.
- Subject 3b being the same subject as 3a after surgical re-opening of the stenosis at the right proximal ICA.

From the above, synthetic 4D Flow MRI data were generated by sampling the nodal CFD output onto a uniform voxelized image grid. With the aim of covering varying spatial scales, data was generated for spatial samplings of dx = 1.5, 1.0, 0.75, 0.5, and 0.375 mm isotropic, respectively (allowing for high/low resolution pairs of 1.5/0.75; 1.0/0.5; and 0.75/0.375 mm). A time step of dt = 10 ms was used in order to increase the amount of input data for training. Data were consistently extracted for a region-of-interest (ROI) centered around the intracranial vessels. An illustration of one of the utilized models is shown in Fig. 2.

2.2.2. Cerebrovascular in-vivo data

Using a cohort of 8 healthy volunteers (2 women, 6 men, 55 ± 18 years), MRI acquisitions were performed at 3T (Siemens Magnetom Skyra, Erlangen, Germany) using a 20-channel head/neck coil. Centering a ROI around the CoW, acquisitions started with a TOF MRA sequence (TR = 21 ms; TE = 3.6 ms; flip angle = 18°), followed by 4D Flow MRI (prospective *k-t* GRAPPA dual-venc (130/45 cm/s) acquisitions (Schnell et al., 2017), dt = 95–104 ms). Flow images were acquired at two different resolutions: dx = 1.1 mm isotropic, and dx = 0.8 mm isotropic. Scan times were 10–15 min for all sequences, respectively. In all instances, data was corrected for concomitant gradient fields, eddy currents, and noise. All clinical acquisitions followed institutional review board (IRB) approval and informed consent.

2.2.3. Patch generation

To enhance clinical relevance of the training data, synthetic 4D Flow MRI from Section 2.2.1 were transformed into clinical-level equivalents. In short, realistic velocity-to-noise ratios (VNR) were extracted from the clinically acquired data in Section 2.2.2, equaling approximately VNR = 5.67 ± 1.64 at dx = 1.1 mm, and VNR = 2.97 ± 0.78 at dx = 0.8 mm. With simulated data from Section 2.2.1 treated as effective phase information, and with clinically acquired magnitude data from Section 2.2.2 used as reference, clinical-level noise was added to the synthetic 4D Flow MRI through k-space downsampling, extracting complex numbers from the synthetic phase and clinical magnitude images, respectively. Note that such noise was added to the low-resolution dataset only, resulting in a network tasked not only with increasing resolution, but also removing noise.

To generate a larger number of training sets from the limited ($n = 4$) number of models, the FOV was split into 3D patches of restricted spatial extent. Specifically, from each temporal frame patches of 12^3 voxels were extracted from random positions within the FOV (enforcing a minimum flow region of >5%). Additionally, patches at different resolution pairs (1.5/0.75 mm; 1.0/0.5 mm; 0.75/0.375 mm; as per Section 2.2.1) were used to train the network, effectively increasing the internal resolution and different vessel sizes learned by the network. The training was thus performed in a supervised fashion, with both low and high-resolution 3D patches exposed to the network during training. Visualization of the distribution of patches is shown in Fig. 2. For every patch, data augmentation by rigid cartesian rotations (90/180/270°) was applied to avoid directional bias, with the number of rotations determined during preliminary data evaluation (additional levels of rotations were not assessed considering computational demands during training).

Data from Subjects 1 and 2 were selected for training with 10 patches per temporal frame selected generating a total of 42,900 patches. Subject 3a was selected for validation, with 2 patches per frame selected generating a total of 2730 patches. Subject 3b was withheld completely for testing. Based on preliminary analysis, training was performed for 60 epochs to reach empirical convergence, with the aforementioned continuous validation tests and incorporated weight regularization utilized to avoid overfitting. With training performed on a Titan X GPU with 12GB memory, each epoch lasted approximately 30 min, rendering complete training in about 30 h. Super-resolved velocity fields were predicted on a patch-basis, with complete volumes reconstructed by stitching patches together. At the low-resolution input, patches were extracted with a stride of $s = n$ - 4 voxels in each Cartesian direction, with n being an arbitrary patch size configurable during inference. As a result, two voxels from each side of the patch were overlapping with neighboring patches. At the super-resolved output, these overlaps were therefore discarded to avoid edge artifacts. Note that $2r$ voxels were stripped from each patch side, reducing data to the patch center, with r being the selected upsampling ratio.

2.3. Validation of super-resolution performance, and recovery of cerebrovascular relative pressure

2.3.1. In-silico validation

To validate performance of the super-resolution network, the *in-silico* models and corresponding synthetic 4D Flow MRI data from Section 2.2.1 was utilized. Performance was evaluated with respect to both super-resolved velocity fields and derived flows, as well as functional recovery of relative pressures using coupled physics-informed image processing.

2.3.1.1. Super-resolution velocity and flow validation. For the super-resolved velocity fields, linear regression analysis was performed against reference high-resolution velocity data from the CFD analysis, assessing Cartesian velocity components and velocity magnitudes separately. Bland-Altman plots of the same data were also extracted to assess potential network bias. For general quantification, assessment of root mean square error (RMSE), cosine similarity, absolute magnitude error, and relative magnitude error were all performed, with the latter extracted as per

$$\varepsilon = \frac{1}{N}\sum_{i=1}^{N}\frac{\sqrt{\Delta v_x^2 + \Delta v_y^2 + \Delta v_z^2}}{|v|} \tag{3}$$

with Δv_x^2, Δv_y^2, and Δv_z^2 being Cartesian velocity components.

Furthermore, flow rates through three different planes cutting through sections of the right ICA, mid-ICA, and MCA were also compared between super-resolved and high-resolution reference synthetic 4D Flow MRI data. Quantification of RMSE and relative error, respectively, were also performed against high-resolution reference flow from the CFD analysis.

For both velocity and flow, differences between low, high, and super-resolved datasets were statistically quantified using a two-sided Wilcoxon rank sum test using a significance level of $p < 0.05$.

2.3.1.2. Super-resolution relative pressure validation. A key component of our study was to assess whether network-based super-resolution images also enabled accurate extraction of conjunctive, functional relative pressures. A variety of methods exist to derive relative pressures from image velocity data, each with specific method assumptions and applicability in the cerebrovascular space. Here we use the virtual work-energy relative pressure (vWERP) method, which allows for arbitrary probing through narrow and bifurcating structures (Marlevi et al., 2019), with catheter-based validation underlining the method's potential. vWERP has also been applied in a cerebrovascular setting, indicating promising abilities whilst highlighting the importance of sufficient spatial resolution (Marlevi et al., 2021b).

With details provided in previous work (Marlevi et al., 2019), vWERP originates from a virtual work-energy form of the Navier-Stokes equations, derived by introducing an auxiliary virtual field w, and evaluating the resulting expression over the fluid domain of interest, Ω. Doing so, relative pressures can be derived as:

$$\Delta p = -\frac{1}{Q}\left(\frac{\partial K_e}{\partial t} + A_e + V_e\right) \tag{4}$$

with

$$K_e = \rho\int_{\Omega} v\cdot w\, d\Omega;\ A_e = \rho\int_{\Omega}(v\cdot\nabla v)\cdot w\, d\Omega;\ V_e = \mu\int_{\Omega}\nabla v : \nabla w\, d\Omega;\ Q = \int_{\Gamma_i} w\cdot n\, d\Gamma \tag{5}$$

Here, each term represents different *virtual* energy components, including virtual kinetic energy (K_e), virtual advective energy rate (A_e), virtual viscous energy dissipation (V_e), and the virtual flow (Q) going through a selected inlet plane (Γ_i). Introducing w as a divergence-free field with $w = 0$ at all domain wall boundaries, relative pressures can then be extracted directly from the imaged flow field v.

Using vWERP, relative pressures were estimated over four different cerebrovascular sections in each synthetic 4D Flow MRI dataset, respectively: *left / right ICA*, going from the cranial end of the cervical ICA to the mid-section of the petrous ICA, and *left / right ICA-middle cerebral artery (MCA)*, going from the mid-section of the petrous ICA to midway along the M1-segment of the MCA. Based on previous analysis (Marlevi et al., 2021b), estimations were performed on low/high resolution pairs of 1.0/0.5 and 0.75/0.375 mm, as well as on corresponding super-resolution data. In all instances, data were extracted with temporal sampling of dt = 40 ms, to liken a clinically realistic acquisition.

Just as in Section 2.3.1.1, linear regression analysis was performed for super-resolved relative pressures against reference high-resolution pressure field data originating from the simulated CFD output. Bland-Altman plots were also extracted to assess potential estimation bias. For general quantification, assessment of RMSE, cosine similarity, and relative error was also performed. Consistently, differences between low-, high-, and super-resolved datasets were statistically quantified using a two-sided Wilcoxon rank sum test with significance level of $p < 0.05$.

2.3.1.3. Comparison to alternative super-resolution approaches. To further quantify the performance of the proposed cerebrovascular super-resolution network, results were compared to a few alternative image processing approaches proposed to achieve super-resolution conversion on acquired image sets. Specifically, upsampled super-resolution velocity images were derived using:

- Bilinear interpolation
- Sinc interpolation (by zero padding in k-space)
- The original 4DFlowNet (trained exclusively using aortic patch data)

Here, 1. and 2. served as alternative deterministic super-resolution interpolation approaches, utilized in previous work to benchmark learned super-resolution performance (Ferdian et al., 2020). Further, 3. was included to assess the added value of the cerebrovascular re-training outlined in Section 2.2, as well as serve as a super-resolution comparison. For each approach, super-resolved velocities and relative pressures were derived and quantified as per Sections 2.3.1.2 – 2.3.1.1.

2.3.2. In-vivo implementation

Adding to the validation in Section 2.3.1, super-resolved velocity

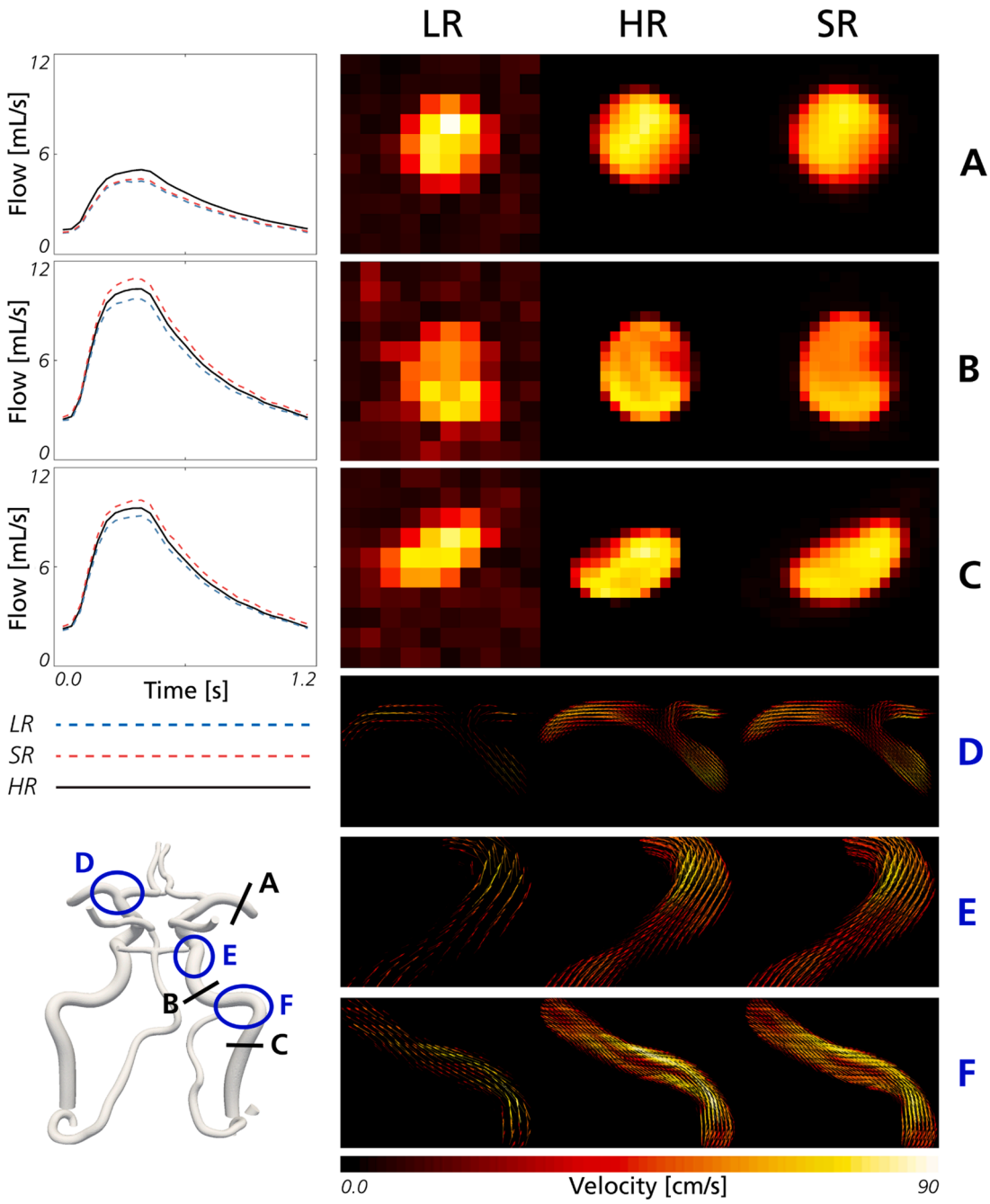

Fig. 3. Comparison between low resolution (LR), high resolution (HR), and super resolution (SR) images at three different intersecting planes (A-C) and three different regional sections (D-F) all through the ICA-MCA. Insets are showing the selected regions in magnified form and with views rotated to highlight velocity vectors. Comparison of flow rates through the intersecting planes (A-C) are also shown. Note that the model insert at the bottom left is shown dorsally.

fields were also generated and assessed in the clinical 4D Flow MRI data from Section 2.2.2. Super-resolution upsampling was performed by a factor of two on all datasets, converting 1.1 to 0.55 mm, and 0.8 to 0.4 mm, respectively. Specifically, this was performed to convert both datasets into a domain where no resolution dependence was to be expected with respect to derived relative pressure estimates (≤0.5 mm required as per Marlevi et al. (Marlevi et al., 2021)).

2.3.2.4. Estimation of super-resolution velocity and flow. Native and super-resolved flow fields were qualitatively compared to assess visual correspondence. Although data was not acquired in integer resolution pairs, through-plane flow rates at the proximal section of the left and right MCAs were still compared between resolution sets to quantify differences between native and super-resolved resolutions, as well as changes in velocity-to-noise ratio (VNR).

2.3.2.5. Estimation of super-resolution relative pressure. To assess relative pressures in the *in-vivo* data, similar ICA-MCA sections as the ones used in the *in-silico* analysis were identified. To achieve this, vessel segmentation was first performed using a previously published analysis framework (Vali et al., 2019). Second, inlet and outlet planes for the relative pressure estimations were positioned based on relevant anatomical landmarks along the right and left ICA and MCA, with planes visually co-aligned between resolutions (1.1 and 0.8 mm, respectively). With planes and segmentations created, *v*WERP was used to extract relative pressures in all subjects. Whilst lacking reference pressures,

Table 1
Flow rate measurements on Subject 3b for the right MCA, mid-ICA, and ICA. For all sections, results were measured by averaging 3 parallel cross-sectional slices.

Plane	LR flow rate [mL/s]	SR flow rate [mL/s]	HR flow rate [mL/s]	SR-HR flow rate [mL/s]	Rel. diff. [%]
A	2.71 ± 1.1	2.80 ± 1.1	3.13 ± 1.2	−0.33 ± 0.1	10.3 ± 0.9
B	5.63 ± 2.6	6.29 ± 2.9	5.95 ± 2.8	0.34 ± 0.2	5.8 ± 0.5
C	5.24 ± 2.4	5.83 ± 2.7	5.50 ± 2.6	0.33 ± 0.1	6.4 ± 1.2

extracted measures were compared over different resolutions, assessing linear correlations and Bland-Altman plots between the different sets (with and without super-resolution, respectively). Differences between datasets were statistically quantified using a two-sided Wilcoxon rank sum test with a significance level of $p < 0.05$.

3. Results

3.1. In-silico validation of super-resolution 4D flow MRI

3.1.1. Super-resolution velocity and flow validation

Complete evaluation was performed on the one test subject (Subject 3b), using 1 mm input data (low resolution, LR) to generate super-resolution equivalents at 0.5 mm (super resolution, SR), comparing output quality against high-resolution (HR) reference data at the same 0.5 mm resolution. As apparent in Fig. 3, significant noise reduction is achieved in the SR velocity fields. Furthermore, SR flow rates indicate slight overestimation at the proximal-most (A) section (mean shift of −0.33 ± 0.14 mL/s), whilst showing a similar but opposite underestimation of flow in the more distal (B) and (C) sections (0.34 ± 0.16 mL/s, and 0.33 ± 0.12 mL/s, respectively). Relative differences are however kept <10.3% over the evaluated sections (Fig. 3 and Table 1), and no statistical difference can be inferred when comparing SR and reference HR data ($p = 0.94$ across the complete cardiac cycle).

Isolating peak flow rates in all models, slight error reduction is seen for conversion from LR (RMSE = 0.74 mL/s, relative error = 9.0 ± 6.2%) to SR (RMSE = 0.56 mL/s, relative error = 6.6 ± 4.7%), however, neither LR nor SR data differs significantly from the HR reference ($p = 1.00$ for SR vs. HR; $p = 0.70$ for LR vs. HR).

Fig. 4 shows linear regression plots and Bland-Altman representations for generated super-resolution velocities. In general, excellent correlations are observed between SR and HR velocities, with linear regression slopes and correlation coefficients of $k>0.91$ and $R^2>0.95$ reported for the vessel core region (all voxels apart from the outermost fluid layer), and $k>0.90$ and $R^2>0.72$ for the vessel wall region (the outermost layer of fluid voxels). For the vessel core, no statistical difference can be inferred between SR and HR data ($p>0.15$ across all velocity components). For the vessel wall, significant differences are observed in the out-of-plane direction ($p>0.46$ for v_x and v_y; $p = 0.007$ for v_z).

Slightly lower visual correspondence are seen for velocity magnitudes ($k = 0.82$ and $R^2=0.78$ for core; $k = 0.69$ and $R^2=0.44$ for wall), with both core and wall velocities differing statistically from the HR reference ($p<0.001$). Still, the Bland-Altman output seems to support the quality of the results, with minimal bias indicated (consistent deviations of <0.02 m/s).

Isolating peak velocity magnitudes, measures in both vessel core (RMSE = 0.08 m/s, relative error = 11.0 ± 13.6%, cosine similarity = 0.99 ± 0.07) and vessel wall regions (RMSE = 0.16 m/s, mean absolute error (MAE) = 0.12 ± 0.11 m/s, and cosine similarity = 0.95 ± 0.12) confirm the trends noted above. Similar numbers are also observed for 0.75/0.375 mm resolution sets, as shown in Appendix B.

3.1.2. Super-resolution relative pressure validation

Fig. 5 shows linear regression and Bland-Altman plots for estimations of relative pressure across different resolutions and all models (example relative pressure traces are also given in Appendix C). Overall, significant underestimation is observed at LR (1 mm, $p<0.001$ for LR vs. SR), while accurate estimates are reported at the HR (0.5 mm) setting. Importantly, distinct improvements in functional relative pressures are observed for the super-resolved velocity fields as compared to the LR input: relative error in peak relative pressure decreasing from 23.3 ± 14.9% at LR, to 11.0 ± 7.3% at SR, with 5.1 ± 2.3% at reference HR. Similarly, the RMSE for the entire time series goes from 1.1 ± 1.7 mmHg at LR, to 0.3 ± 0.2 mmHg at SR, compared to 0.2 ± 0.1 mmHg at HR. Conversion into SR also mitigates any statistically significant difference

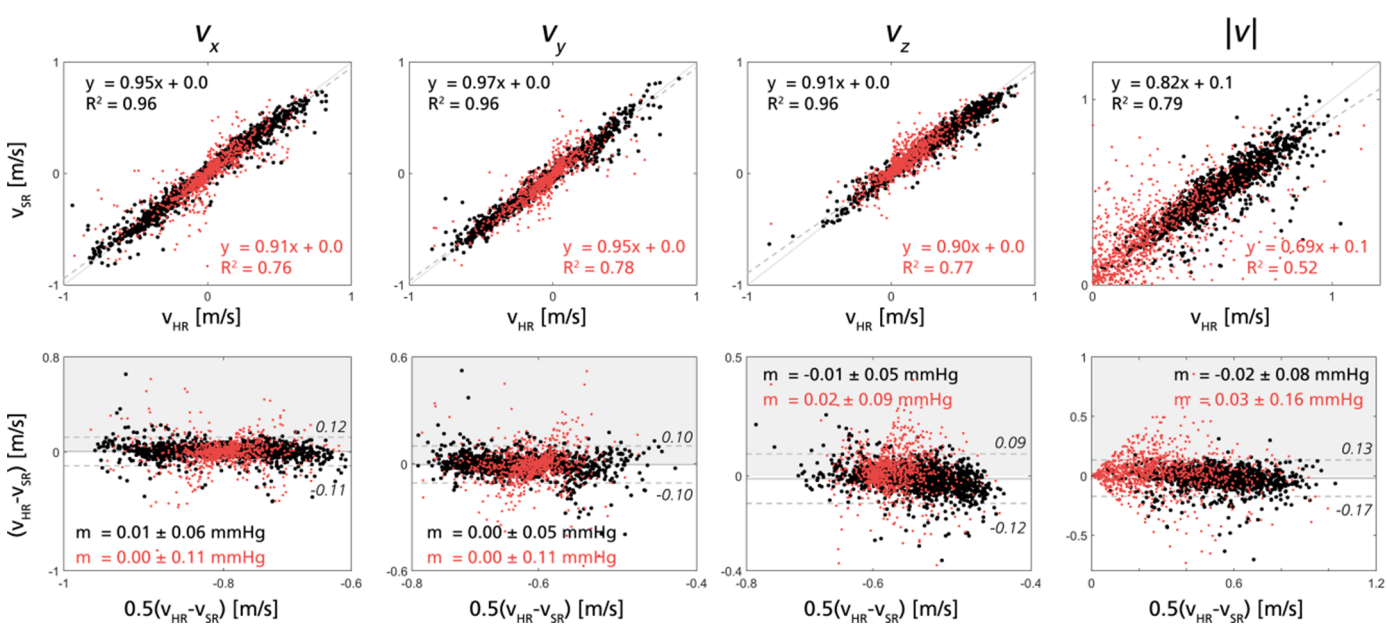

Fig. 4. Top: Regression plot for each of the velocity components (vx, vy, and vz) and velocity magnitude between ground truth and super-resolved image during the peak flow for in-silico test case (Subject 3b). Bottom: Bland-Altman plot for each of the velocity components during peak flow. The plots show 5% of the data points (randomly selected) within the vessel core (black) and vessel wall (red), respectively.

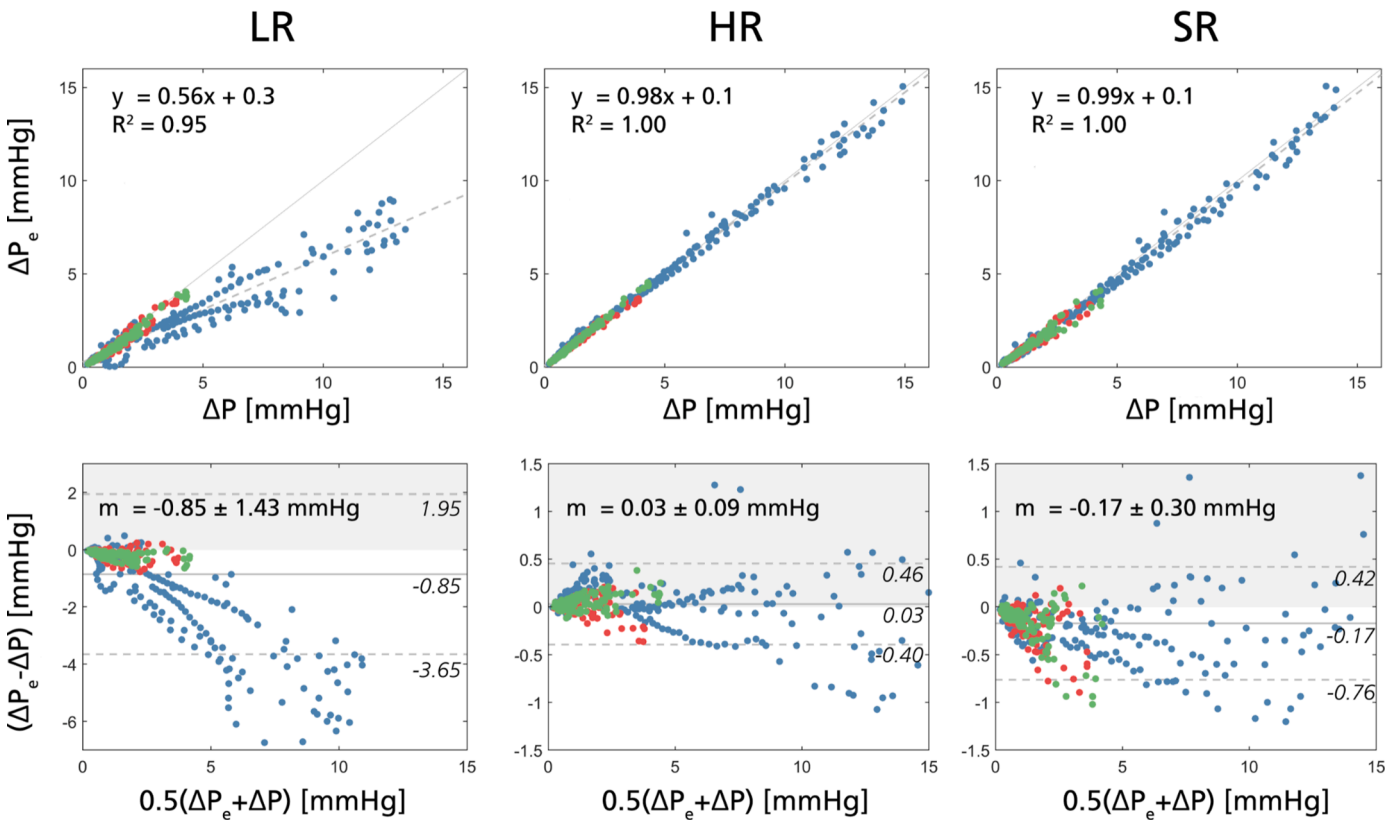

Fig. 5. Linear regression (top row) and Bland-Altman plots (bottom row), comparing relative pressure estimates to reference CFD equivalents using low resolution data (LR, 1 mm, left column), high resolution data (HR, 0.5 mm, middle column), and super-resolution data (SR, converting 1 mm to 0.5 mm, right column). The colors depict different data sets (training in blue (Subject 1 and 2), validation in red (Subject 3a), testing in green (Subject 3b)).

Table 2
Image-based peak relative pressure measurements through the right ICA-MCA section for all different subjects.

Model	LR peak Δp [mmHg]	SR peak Δp [mmHg]	HR peak Δp [mmHg]	SR-HR peak Δp [mmHg]	Rel. diff. [%]
1	7.39	13.93	13.11	14.04	0.82
2	6.78	12.97	12.51	13.00	0.46
3a	2.51	2.91	2.81	2.88	0.10
3b	2.35	2.80	2.66	2.71	0.14

against the HR data ($p = 0.08$ for SR vs. HR). Quantitative output for ICA-MCA sections across all different models are given in Table 2.

The above is confirmed in Fig. 5 with conversion from LR to SR increasing the linear regression slope from $k = 0.56$ to 0.99, representing a virtual 1:1 correlation to ground truth relative pressures ($k = 0.98$ at HR for reference). Likewise, the mean bias shift in the LR set (mean shift of -0.85 ± 1.43 mmHg) is significantly reduced by conversion into SR data (mean shift of -0.17 ± 0.30 mmHg). The HR data observes no estimation bias (mean shift of 0.03 ± 0.22 mmHg). Notice that similar improvements are observed when converting 0.75 mm base resolution sets into super-resolution equivalents (at 0.375 mm), with complete data for this analysis shown in Appendix B.

3.1.3. Comparison to alternative super-resolution approaches

For the comparison against alternative image processing approaches, complete results are provided in Appendix D. In brief, super-resolved velocities obtained by deterministic bilinear interpolation show higher deviations from ground truth HR data, with linear regression slopes and correlation coefficients consistently lower than what was observed with the cerebrovascular 4DFlowNet (k>0.70 and R^2>0.56, and k>0.42 and R^2>0.37 observed for vessel core and wall regions, respectively). Statistical differences between bilinear interpolation and HR reference velocities can also be inferred for some vessel core entries ($p < 0.001$ for both v_x and v_{mag}). Similar deviations are also observed for the trained aortic network with accuracy lower than the cerebrovascular 4DFlowNet (k>0.73 and R^2>0.62, and k>0.51 and R^2>0.35 observed for vessel core and wall regions, respectively) and with statistical differences inferred against reference HR data for the velocity magnitude entries (p<0.004 for both core and wall v_{mag}). In comparison, super-resolved velocities obtained by deterministic sinc interpolation exhibits comparable performance to the cerebrovascular 4DFlowNet, even outperforming the learned approach in singular velocity entries (k>0.93 and R^2>0.88, and k>0.66 and R^2>0.79 observed for vessel core and wall regions, respectively). As for the cerebrovascular 4DFlowNet, the sinc interpolation shows no statistical differences against HR data in the vessel core (p>0.20 across all velocity components), however, deviations are inferred in the out-of-plane direction of the vessel wall component (p>0.79 for v_x and v_y; $p = 0.002$ for v_z).

Continuing into estimations of cerebrovascular relative pressures, key results are provided in Fig. 6. As shown, all alternative approaches exhibit varying degrees of underestimation bias as compared to the reference HR data ($k = 0.66$ and a mean bias shift of -0.82 ± 1.13 mmHg for bilinear interpolation; $k = 0.87$ and a mean bias shift of -0.31 ± 0.48 mmHg for sinc interpolation; $k = 0.87$ and a mean bias shift of -0.41 ± 0.58 mmHg for the aortic network). Results are significantly different from HR reference results for bilinear interpolation (p<0.001) and the aortic network ($p = 0.003$), however, no such inference was observed for the sinc interpolation data ($p = 0.15$). Nevertheless, peak relative pressures estimated by deterministic sinc interpolation are consistently higher than what was reported for the cerebrovascular 4DFlowNet approach (relative error of $25.0 \pm 7.3\%$, $9.6 \pm 5.6\%$, and $14.8 \pm 11.9\%$; RMSE of 1.0 ± 1.1 mmHg; 0.4 ± 0.5 mmHg; and $0.5 \pm$

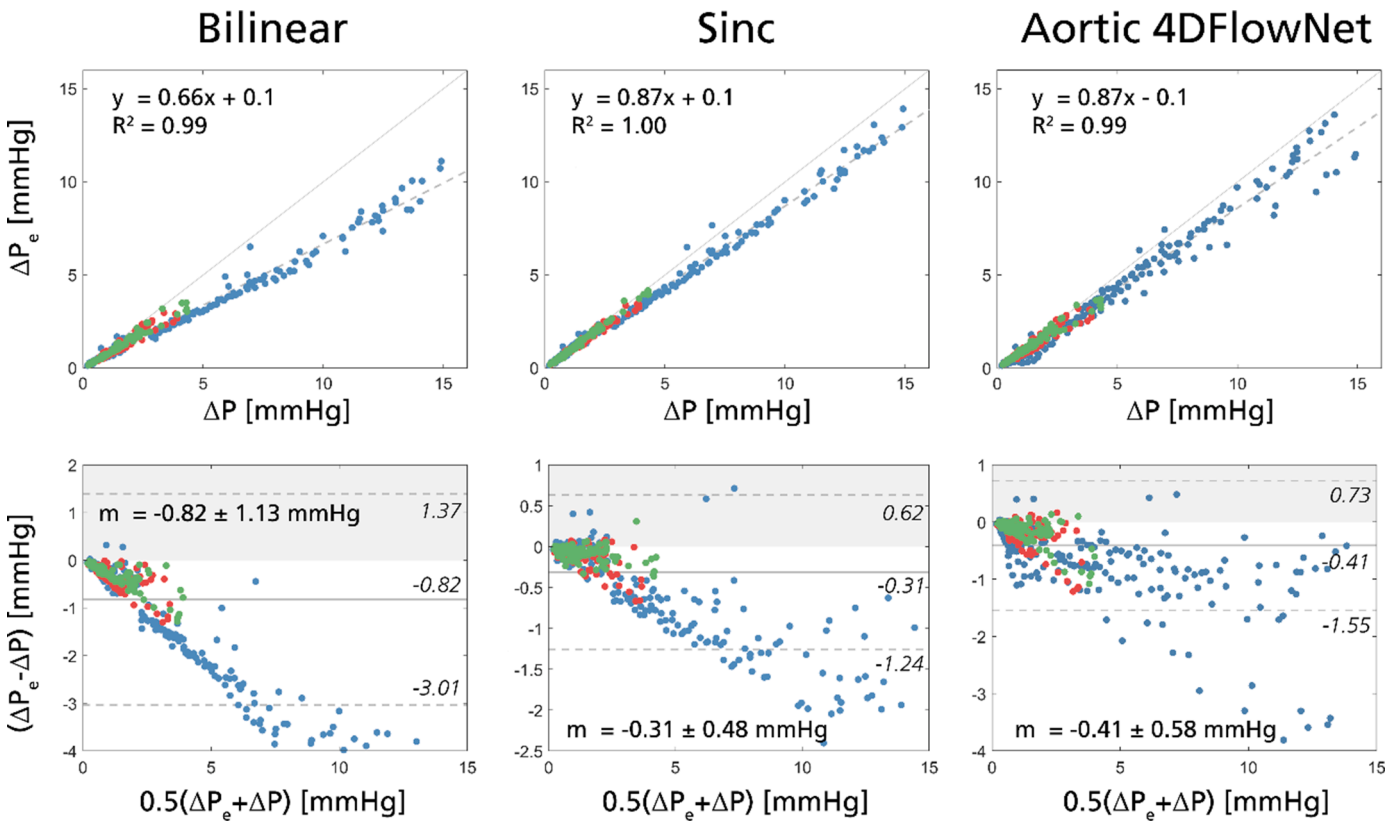

Fig. 6. Linear regression (top row) and Bland-Altman plots (bottom row), comparing relative pressure estimates to reference CFD equivalents using a few alternative super-resolution approaches including bilinear interpolation (left column), sinc interpolation (middle column), and the original 4DFlowNet trained exclusively using large aortic flow patches (right column). The colors depict different data sets (training in blue (Subject 1 and 2), validation in red (Subject 3a), testing in green (Subject 3b)).

0.6 mmHg; for bilinear, sinc, and aortic network, respectively). Complete data for the above is provided in Appendix D.

3.2. *In-vivo implementation*

3.2.1. *Estimation of super-resolution velocity and flow*

For the *in-vivo* dataset, visual inspection confirms qualitative improvement with regards to noise reduction and data appearance of the generated super-resolved 4D Flow MRI data (see Fig. 7). Specifically, VNR show a 4-times increase in the 0.55 mm SR data (going from VNR = 5.67 ± 1.64 at dx = 1.1 mm to VNR 24.20 ± 11.28 at dx = 0.55 mm; $p<0.001$), and a 3-times increase in the 0.4 mm SR data (going from VNR = 2.97 ± 0.78 at dx = 0.8 mm to VNR 9.29 ± 4.25 at dx = 0.4 mm; $p<0.001$).

Assessing flow rates through the left and right MCAs, the clinical base resolution data indicated a flow rate range of 0.65 to 7.13 mL/s and peak flow rates of 4.96 ± 1.52 mL/s at dx = 1.1 mm, compared to a slightly reduced range of 0.67 to 5.53 mL/s and peak flow rates of 3.47 ± 1.01 mL/s at dx = 0.8 mm. Converting to SR equivalents (dx = 0.55 mm and 0.4 mm, respectively) flow rates are only modestly modified, with slight downregulation observed in both datasets (flow range of 0.58 to 6.93 mL/s and peak flow rates of 4.39 ± 1.56 mL/s at dx = 0.55 mm; flow range of 0.64 to 5.13 mL/s and peak flow rates of 3.32 ± 0.91 mL/s at dx = 0.4 mm).

3.2.2. *Estimation of super-resolution relative pressure*

Relative pressures were derived for all *in-vivo* subjects and sections. Overall, estimates were within the range of −0.6 to 6.0 mmHg for the 1.1 mm data, with peak relative pressures at 2.9 ± 1.6 mmHg, compared to a range of −0.1 to 6.8 mmHg for the 0.8 mm data, with peak relative pressures at 3.8 ± 1.8 mmHg. Converting to SR, the ranges changes with estimates getting closer to one another: SR data at dx = 0.55 mm (input at dx = 1.1 mm) exhibiting a range of −0.7 to 5.9 mmHg with peak relative pressures at 2.6 ± 1.4 mmHg; SR data at dx = 0.4 mm (input at dx = 0.8 mm) exhibits a range of −0.5 to 4.3 mmHg with peak relative pressures at 2.9 ± 1.1 mmHg. Note that variations between individual subjects are still present in the super-resolved datasets.

Although lacking *in-vivo* reference pressure, Fig. 8 shows linear regression and Bland-Altman plots comparing LR and HR data to its SR equivalents. At base resolutions (LR vs. HR) a systematic bias shift in relative pressure is observed between the two resolutions ($k = 0.64$; $R^2 = 0.81$; mean shift = −0.93 ± 0.93 mmHg; $p<0.001$). Converting to super-resolved equivalents, the shift is reduced, although without completely recovering a 1:1 correlation between the two datasets ($k = 0.81$; $R^2 = 0.77$; mean shift = −0.47 ± 0.72 mmHg; $p<0.001$).

4. Discussion

In this study, we evaluated the utility of quantitative super-resolution 4D Flow MRI for the accurate assessment of cerebrovascular hemodynamics. Specifically, we showcased how - through a two-step approach of using a re-trained deep residual network (4DFlowNet) and a subsequent physics-informed image processing algorithm (*v*WERP) - super-resolved intracranial velocity fields, regional flows, and functional relative pressures can all be recovered from low-resolution input data, with the proposed approach effectively mitigating estimation biases otherwise observed in the input images. With non-invasive cerebrovascular assessment intrinsically complicated by the narrow and tortuous vasculature, our results highlight the potential of quantitative super-resolution 4D Flow MRI to provide accurate functional cerebrovascular hemodynamic assessment in a clinical setting.

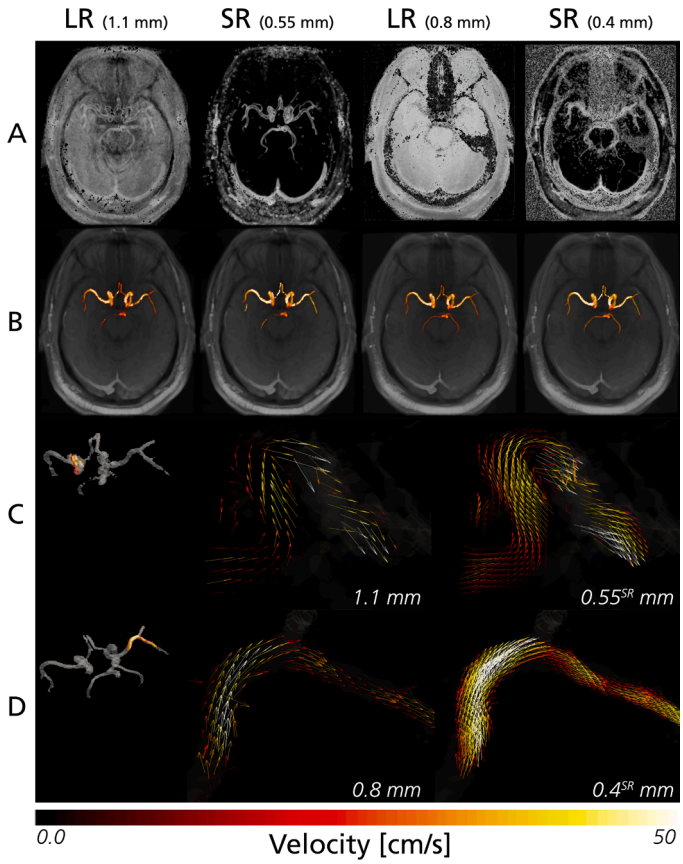

Fig. 7. Visual comparison of an in-vivo case at low (LR) and super-resolution (SR) given for both sets of dx=1.1 and 0.55, and 0.8 and 0.4 mm, respectively. Improvements in VNR are apparent in the super-resolved phase images (A) as well as in the flow visualizations (B). Direct velocity vectors comparison are given for a section through the right MCA for the paired low resolution (1.1 mm)/super-resolution (0.55 mm) in (C), and for the paired low resolution (0.8 mm)/super-resolution (0.4 mm) in (D), with vectors shown projected onto a visual2D plane. In general, broad view of the velocity vectors only reveal minor differences between resolution sets, although detailed view reveals velocity vectors conforming more to the anatomy of the vessel in the super-resolved images, including at the near-wall regions.

4.1. In-silico validation of cerebrovascular super-resolution 4D flow MRI to quantify velocity, flow, and relative pressure

In-silico super-resolved flows and velocity fields both conform closely to high-resolution reference data. For super-resolved velocities, slightly reduced accuracy was identified along near-wall voxels as well as for velocity magnitudes. For near-wall voxels, the behavior is similar to what has been previously reported (Rutkowski et al., 2021), and is not entirely surprising: near-wall voxels suffer from reduced input information (being surrounded by 'information-depleted' static tissue), and will be inherently linked to reduced signal quality. Dedicated neural networks have been explored for the recovery of near-wall velocities in 2D flow data (Wang et al., 2020), although application in 4D Flow MRI data remains to be performed. For velocity magnitudes, the slight reduction in accuracy can instead be attributed to magnitudes not being represented as a separate output channel, with the network instead focusing on recovering individual Cartesian velocity components separately. Errors in individual velocity components will thus be amplified when a magnitude operation is performed, in-line with our obtained results.

In addition to the recovery of super-resolved velocities, a major part of our work focused on whether super-resolution conversion would enable accurate estimation of *functional* relative pressures; an entity directly dependent on utilized spatial resolution (Marlevi et al., 2021b). As reported in Section 3.1.2), the sequential combination of a deep learning based (4DFlowNet) super-resolved images and a physics-informed analysis algorithm (*v*WERP) allow for accurate estimation of cerebrovascular relative pressures. This not only indicates the utility of the *v*WERP algorithm but also highlights that the 4DFlowNet architecture allows for accurate estimation of the complete fluid mechanical environment, with precise recovery of both velocity and velocity gradients needed to accurately extract relative pressures. Importantly, although variations in bias are observed for different modelled subjects at low resolution (more pronounced bias seen for the training subjects 1–2, shown as blue glyphs in Fig. 5), super-resolution conversion consistently resolves relative pressures across all four tested models and anatomies.

Another benefit of the repurposed 4DFlowNet is the ability to significantly improve VNR, showcased in both our *in-silico* and *in-vivo* results. Deterministic multi-venc sequences have been explored to enhance VNR (Schnell et al., 2017), however, using a post-processing super-resolution approach in principle enables maintained signal quality even at reduced scan times, as highlighted in other image-based work (Rutkowski et al., 2021). It is worth noting that although denoising is desired for a range of different use-cases (simplifying segmentation; improving direct velocity or flow estimations; etc.), its impact on the relative pressures estimates derived by *v*WERP is comparably minor. In fact, it has in previous work been shown how *v*WERP – even at high-noise configurations – enables accurate recovery of cerebrovascular relative pressures given sufficient spatial sampling (Marlevi et al., 2021), owing largely to the method's integrative nature and use of a numerical, noise-free virtual field. As such, the denoising component of 4DFlowNet is rather incorporated for simplified clinical use, although its direct role in e.g., improving segmentation accuracy remains to be assessed.

4.2. Comparative performance of cerebrovascular super-resolution 4D flow MRI

The performance of the cerebrovascular 4DFlowNet was also compared to a set of alternative super-resolution approaches. As shown in Section 3.1.3, although variations exist in the quality of super-resolved velocities (with distinct underestimations observed for both deterministic bilinear interpolation and aortic 4DFlowNet), it is within the derivation of functional relative pressures that the main differences can be observed. Specifically, although *all* alternative approaches reduce some of the estimation bias observed in the LR input data, *neither* of the approaches can fully mitigate the underestimation. This should be put in contrast to the cerebrovascular 4DFlowNet approach, where cerebrovascular relative pressure can be recovered with the same level of accuracy as shown in the reference *in-vivo* data. This finding is particularly interesting when comparing the deterministic sinc interpolation to the cerebrovascular 4DFlowNet: both approaches recover velocities at similar accuracies; however, cerebrovascular 4DFlowNet captures relative pressures more accurately. The reason for this discrepancy lies in the non-trivial relationship between velocity and relative pressure given by the governing Navier-Stokes equations. Mapping flow to pressure goes beyond accurately reconstructing individual velocity components, but also requires accurate recovery of spatiotemporal velocity gradients and the spatial distribution of velocities which all contribute to the global momentum balance. In fact, if assessing the overall momentum balance across all alternative approaches (evaluating the Navier-Stokes equations in each flow voxel within the ROI), the cerebrovascular 4DFlowNet data satisfies the governing momentum balance to a higher degree than the sinc interpolated data in all subjects, corroborating the findings observed with respect to recovered relative pressures. This finding speaks to the strengths of dedicated learned approaches, where the underlying hemodynamics of the flow fields are embedded in the super-resolution procedure. This is also in line with previous work

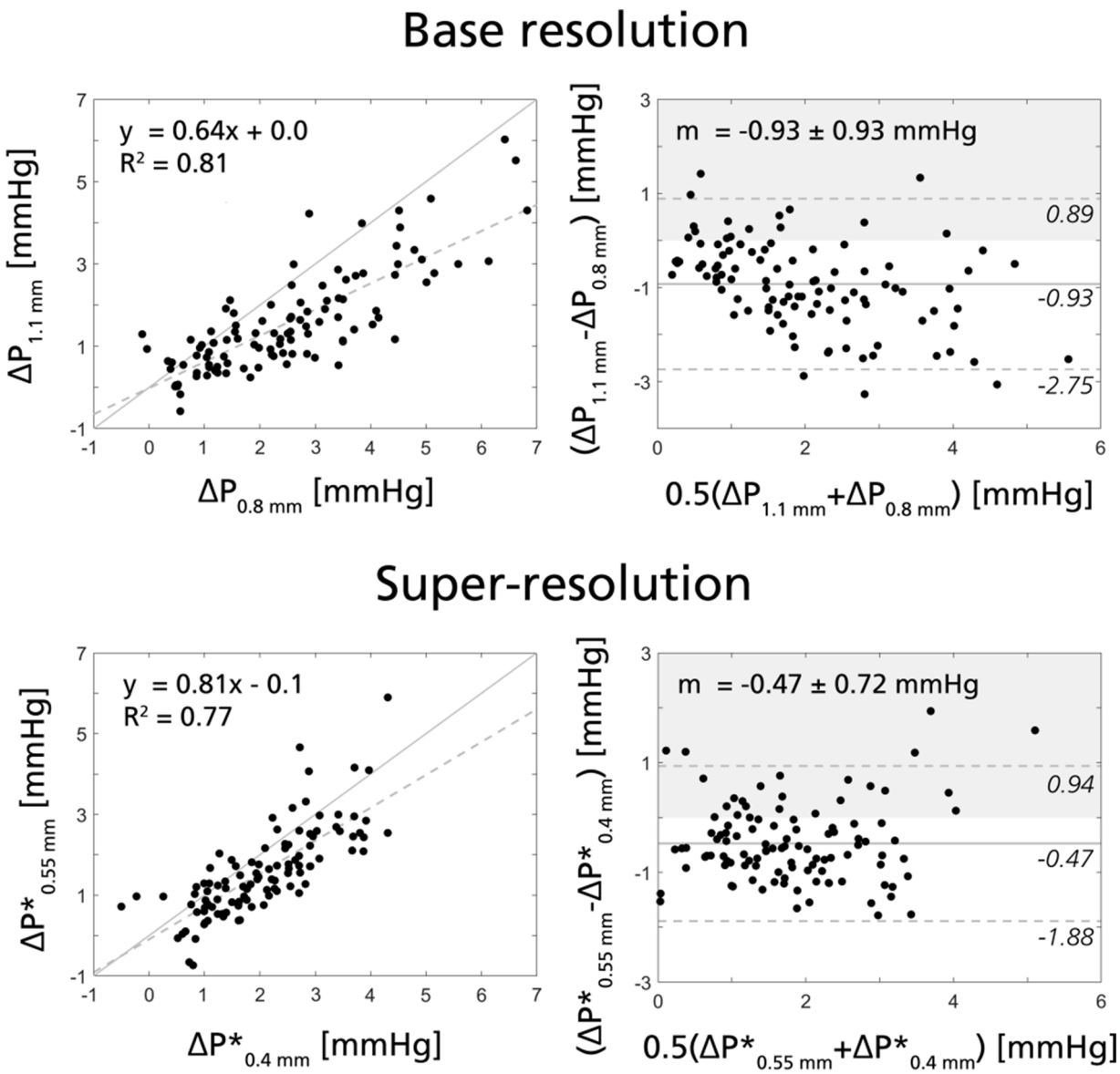

Fig. 8. Linear regression and Bland-Altman plots for the in-vivo cerebrovascular 4D Flow MRI data, showing the relationship between relative pressure estimated at base resolutions (ΔP, upper plots, comparing 1.1 mm and 0.8 mm data) and at equivalent super-resolutions (ΔP*, lower plots, comparing super-resolved 0.55 mm vs. 0.4 mm data).

indicating the added value of learned approaches for achieving effective flow image enhancements, ranging from data denoising and divergence-free corrections to spatiotemporal image enhancement tasks (Rutkowski et al., 2021; Fathi et al., 2020; Kissas et al., 2020; Ferdian et al., 2020). On the contrary, supervised networks might have limited applicability when being brought beyond the well-defined setting in which they were trained, not least being highlighted by our need to re-train the original aortic 4DFlowNet into the cerebrovascular space (see details below in Section 4.3). Still, the larger impact of such data dependence will have to be explored in separate, future work.

As a note on comparative performance, it is worth highlighting that the presented cerebrovascular 4DFlowNet and *v*WERP approach was not compared against alternative learned network approaches. Whilst such head-to-head evaluations would be of direct interest to the community, its numerical implementation remains non-trivial with key alternative networks not yet made publicly available. The varying settings in which alternative networks have been trained also make direct comparison cumbersome and validated benchmark networks remain lacking within the specific field of cerebrovascular flow imaging (notes on the conceptual layout of our presented approach, as compared to alternative state-of-the-art learned approaches, are however provided in Section 4.5).

Lastly, whilst we attempt super-resolution conversion by means of image processing alone, a variety of approaches exist where super-resolution is achieved by means of refined image *acquisition*, utilizing e.g. sub-pixel acquisition shifts or iterative reconstruction algorithms to enhance resulting image resolution (Van Reeth et al., 2012). Whilst such methods cannot be applied in the setting of standard 4D Flow acquisitions, a comparison between pre- and post-processing super-resolution techniques would be a valuable topic for future work.

4.3. *The value of re-training 4DFlowNet for cerebrovascular usage*

The comparison of different approaches (Section 3.1.3) also highlights the importance of re-training, where distinct performance differences are observed when comparing the original (aortic) and repurposed (cerebrovascular) 4DFlowNet. Here, it is important to appreciate the fundamental differences in input training data that exist between the

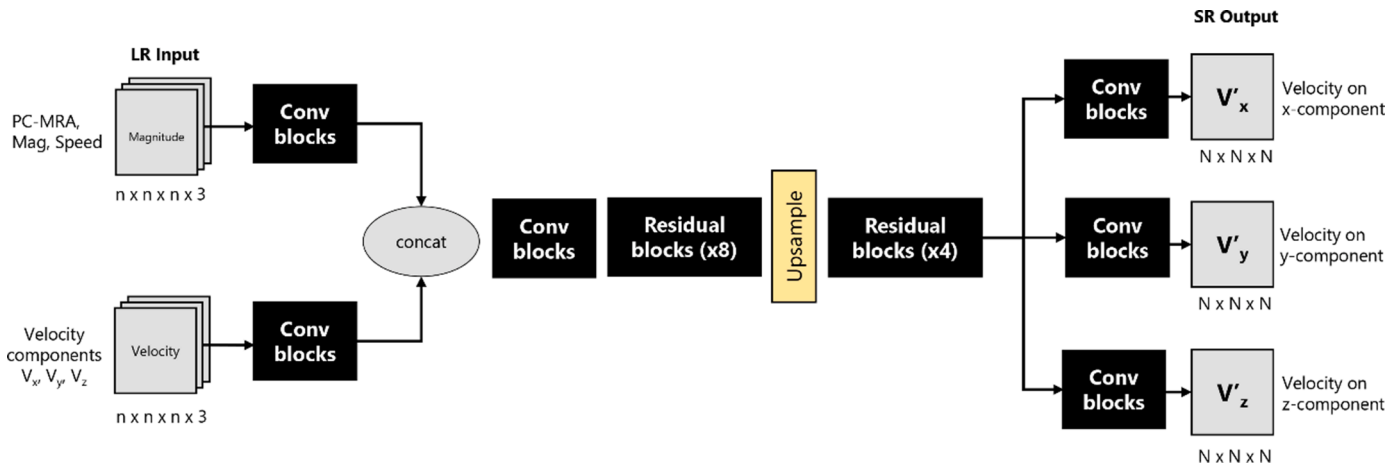

Fig. A.1. General 4DFlowNet architecture, being in principle identical to the original published work on large aortic flows (Ferdian et al., 2020). The network uses two input paths including both magnitude (top) and phase (bottom) information, split into separate Cartesian components. A central upsampling layer is then surrounded by a series of convolutional blocks including symmetric padding and a rectifier non-linearity (ReLU) layer. Network output is then split into three channels, generating super-resolved phase (velocity) information in all Cartesian directions, respectively.

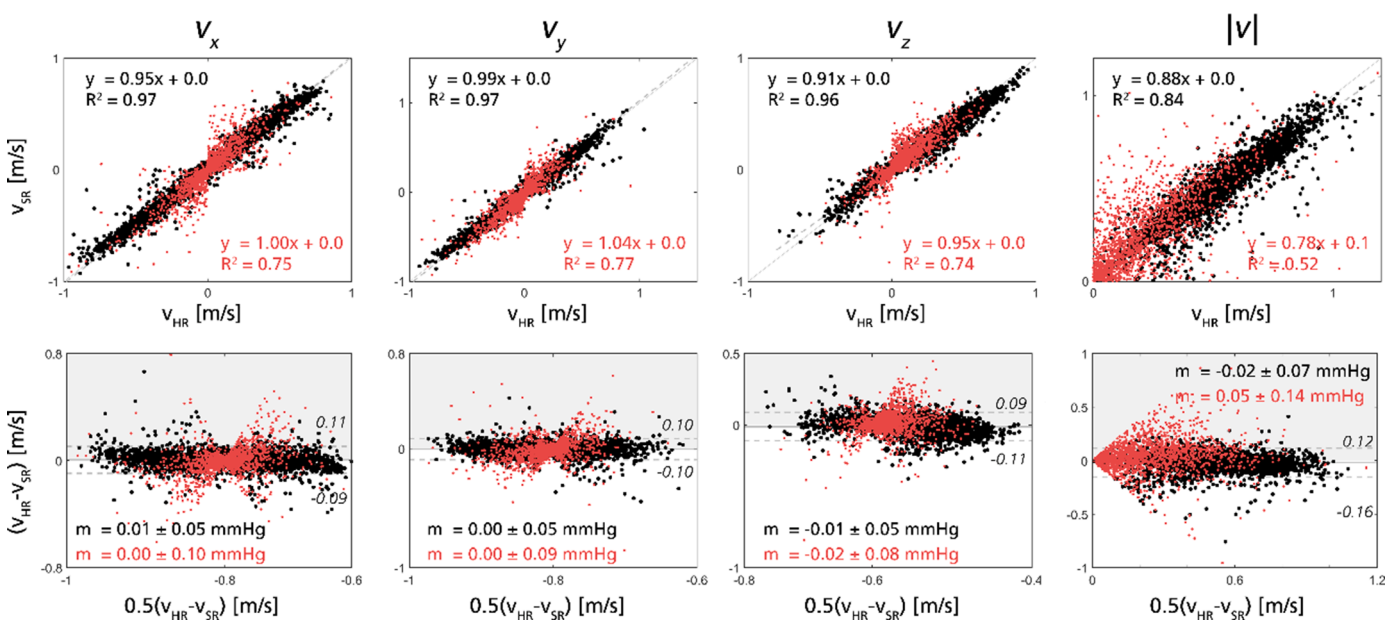

Fig. B.1. Regression plot for each of the velocity components (Vx, Vy, and Vz) and velocity magnitude between ground truth and super-resolved image during the peak flow for the in-silico test case (Subject 3b), using the additional resolution set of 0.75 mm (LR) and 0.375 mm (SR). Bottom: Bland-Altman plot for each of the velocity components during peak flow. The plots show 5% of the data points (randomly selected) within the vessel core (black) and vessel wall (red), respectively.

aortic and the cerebrovascular 4DFlowNet. In the original work, patches containing purely aortic flows from CFD were shown during training, with hemodynamics dominated by transient flows (Lamata et al., 2014) guided through a large vessel structure. On the contrary, cerebrovascular hemodynamics is a joint resultant of transient, advective, and viscous behavior (Marlevi et al., 2021b), with flow restricted by the narrow, tortuous vasculature. Additionally, the cerebrovascular training data contain synthetically generated magnitude images, as such carrying more realistic image properties and noise characteristics. Hence, the original network was never exposed to patches containing the same image characteristics (with tissue regions), or entailing similarly small vessels or tortuous near-wall gradients, and performance is likely reduced when attempting cerebrovascular data recovery.

The fact that re-training resolved estimation bias also demonstrates that the core 4DFlowNet architecture is robust to different types of flows, and that it is rather the information contained in the training data (i.e., vessel sizes, noise characteristics) that determines final performance. Furthermore, we introduced different resolution pairs as training data, which effectively enriched the internal resolution learned by the network. On top of that, changing the resolution while keeping the patch size in the same dimension (12-voxel cube) acted as a surrogate for the different vessel sizes seen by the network. This also indicates that further re-training might be necessary if attempting super-resolution imaging in yet another cardiovascular domain (e.g., intracardiac flow fields), although as long as anatomical structures are similar in size (e.g., cerebral vs. hepatic vessels) maintained accuracy is plausible. To overcome the need for constant retraining, one could envision combining training data from multiple domains to create a network handling both large and small vessel anatomies, as well as fast and slow flows. The performance of such a network, however, remains to be determined.

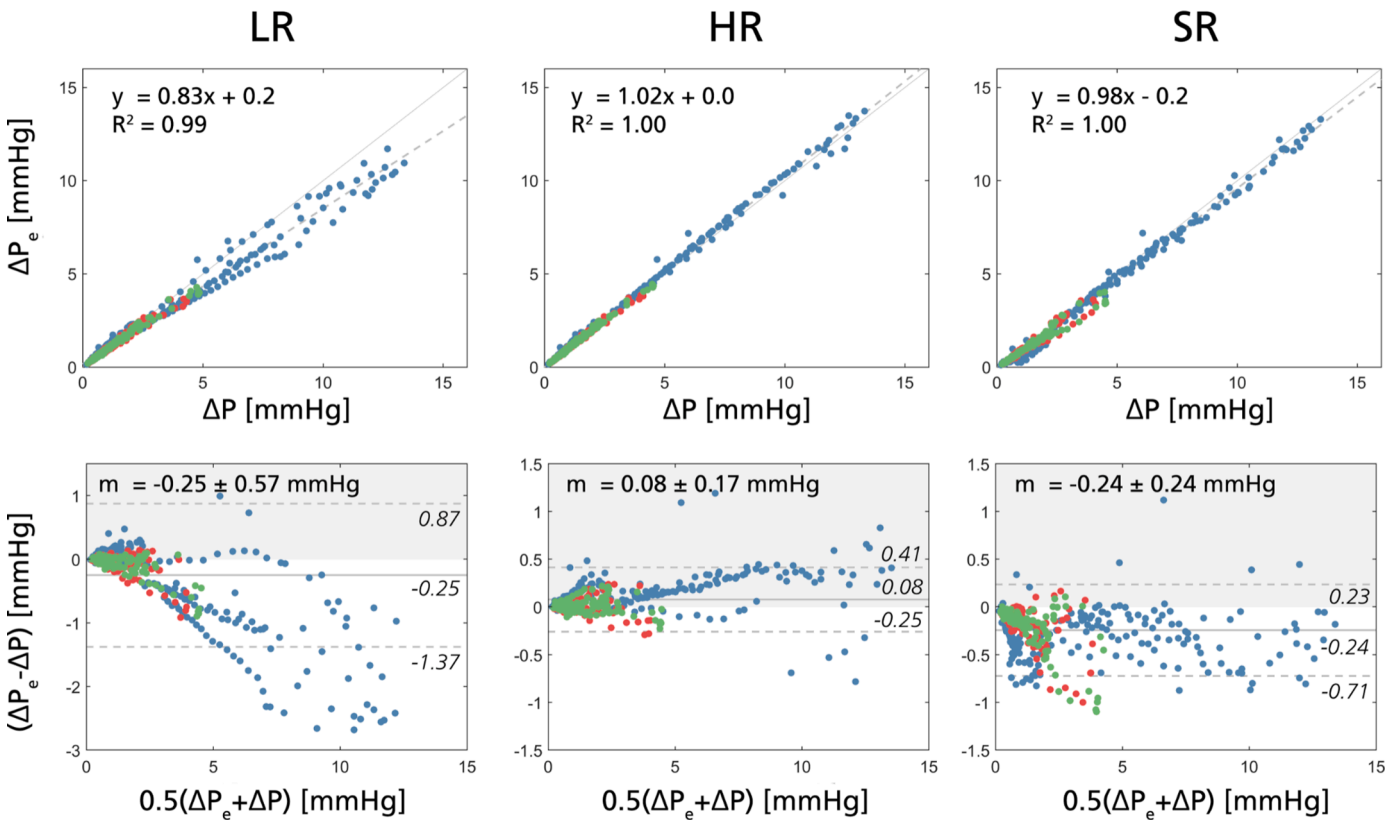

Fig. B.2. Linear regression (top row) and Bland-Altman plots (bottom row), comparing relative pressure estimates to reference CFD equivalents using low-resolution data (LR, 1 mm, left column), high-resolution data (HR, 0.5 mm, middle column), and super-resolution data (SR, converting 1 mm to 0.5 mm, right column). The colors depict different model sets (training in blue (Subject 1 and 2), validation in red (Subject 3a), testing in green (Subject 3b)).

4.4. In-vivo feasibility of cerebrovascular super-resolution 4D flow MRI to quantify flow, velocity, and relative pressure

In Section 3.2, super-resolution images and functional relative pressure estimations were performed in a select *in-vivo* cohort. Although ground truth high-resolution scans or reference pressure measurements were unavailable, the behavior indicated *in-silico* seems replicated *in-vivo*. Specifically, super-resolved flow fields did not introduce any bias shifts, and estimates of both flows and relative pressures indicate slight convergence at upsampled resolutions (note that both datasets were compared at a super-resolution state, to enable comparisons at a reference resolution where no pronounced bias should prevail with respect to estimated relative pressures (Marlevi et al., 2021)). Nevertheless, even though derived relative pressure magnitudes coincide with what has been reported in previous cerebrovascular work (Han et al., 2016), a desired 1:1 relation between resolutions is not achieved. Here, comparably coarse temporal resolution (dt≥95 ms), cardiovascular variations between scans, or temporal intra-scan mismatch could all contribute to this slight discrepancy. Further validation of *in-vivo* work would be beneficial to understand the clinical translation of the combined 4DFlowNet and *v*WERP approach.

4.5. Contextualizing cerebrovascular super-resolution 4D flow MRI

It is worth contrasting our repurposed 4DFlowNet to previously published work within the same space. Whilst few studies exist attempting super-resolution or noise-free recovery of directly imaged flow (Ferdian et al., 2020; Rutkowski et al., 2021), only a handful have attempted the same for *functional* hemodynamic recovery. Kissas et al. (Kissas et al., 2020) proposed a PINN-based network to recover *absolute* pressure in simplified arterial model sections; however, application in cerebrovascular geometries was never attempted. Shit et al. (Shit et al., 2021) similarly proposed the PINN-based 'Velocity-to-Pressure' net; however, super-resolution abilities were never included. In comparison, our work combines the super-resolution utility of 4DFlowNet with the functional recovery of the physics-informed deterministic *v*WERP approach, being previously benchmarked across different cardiovascular domains, including the cerebrovasculature (Marlevi et al., 2021a, 2019, 2021b).

Continuing into the cerebrovascular space, a few very recent works have shown how merging physics-informed analysis, machine learning, and imaging can have particular promise for improving non-invasive cerebrovascular assessment. Fathi et al. (Fathi et al., 2020) used a patient-specific PINN to recover regional flow and pressure from input 4D Flow MRI, promising virtually unrestricted spatiotemporal refinements on recovered velocity fields. However, PINN-based methods are still under active development, with a key main limitation being its dependency on certain pre-defined initial conditions (domain definition, boundary settings, etc.). Similarly, Rutkowski et al. (Rutkowski et al., 2021) recently presented a CNN-based network to reconstruct denoised high resolution 4D Flow MRI in a cerebrovascular setting, using patient-specific *in-vitro* models for both training and testing. However, this method did not offer super-resolution utilities, and did not seem to qualitatively remove noise to the extent observed in our results. One reason to this might be that the network did not consider the inclusion of magnitude image as an input, providing additional information relating to vessel and static tissue region definitions. Along these very same lines, our work also highlights the significant potential of super-resolution 4D Flow MRI in the cerebrovascular space. Within this setting, our study extends these previous works by showing how a two-step application of super-resolution utilities with the physics-informed *v*WERP algorithm provides accurate recovery of relative pressures, overcoming inherent resolution biases otherwise observed in clinical-level image sets (Marlevi et al., 2021b) and allowing for the accurate recovery of this

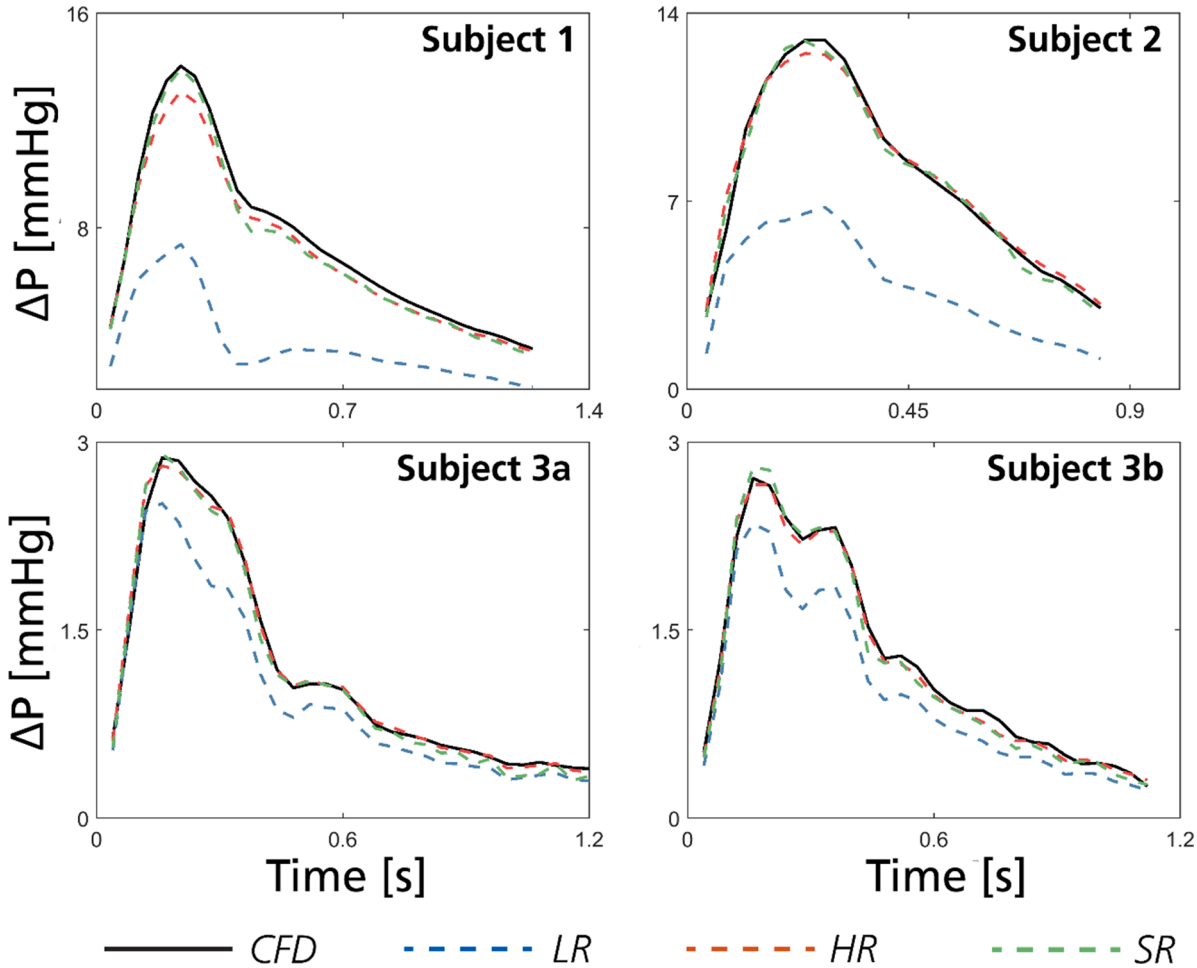

Fig. C.1. Estimated relative pressures through the right ICA-MCA section in all subjects (left to right showing Subject 1, Subject 2, Subject 3a, and Subject 3b). In each graph, relative pressure estimates are derived from low-resolution data in blue (LR, 1 mm), high-resolution data in red (HR, 0.5 mm), super-resolved data in green (SR, converting 1 mm to 0.5 mm). True estimates are given by voxelized equivalents of the CFD pressure field generated at the HR sampling in black.

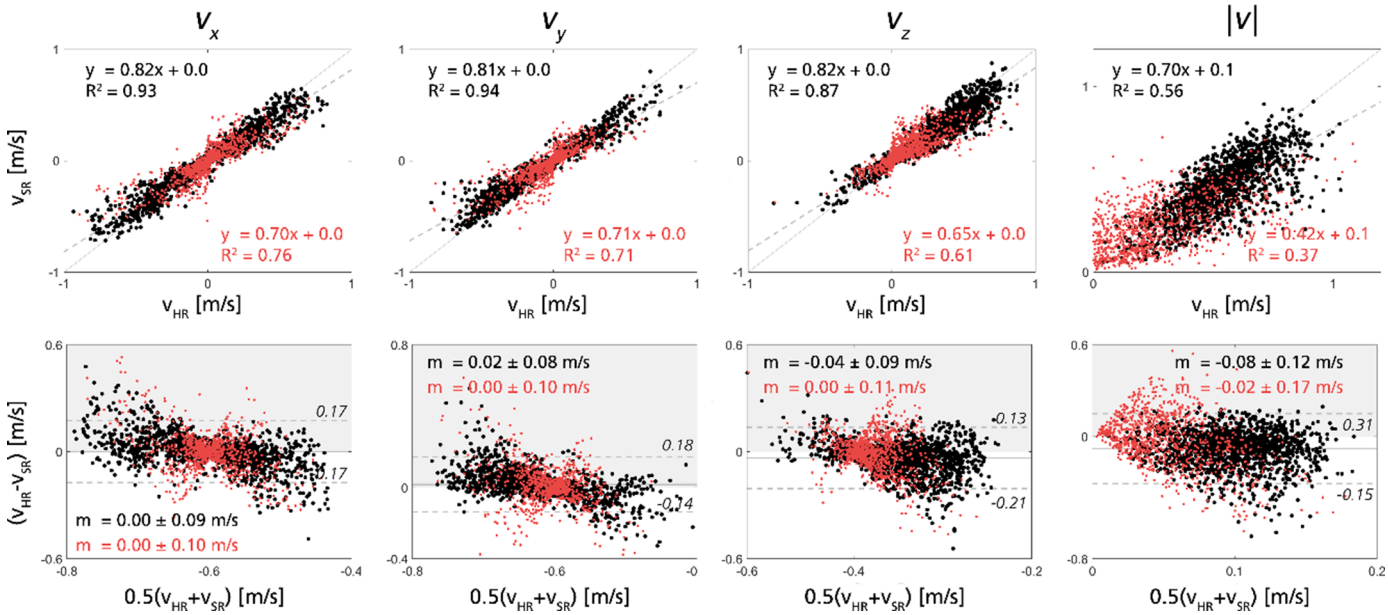

Fig. D.1. Top: Regression plot for each of the velocity components (Vx, Vy, and Vz) and velocity magnitude between ground truth and super-resolved image during the peak flow for the in-silico test case (Subject 3b). Bottom: Bland-Altman plot for each of the velocity components during peak flow. The plots show 5% of the data points (randomly selected) within the vessel core (black) and vessel wall (red), respectively. All data was generated using deterministic bilinear upsampling.

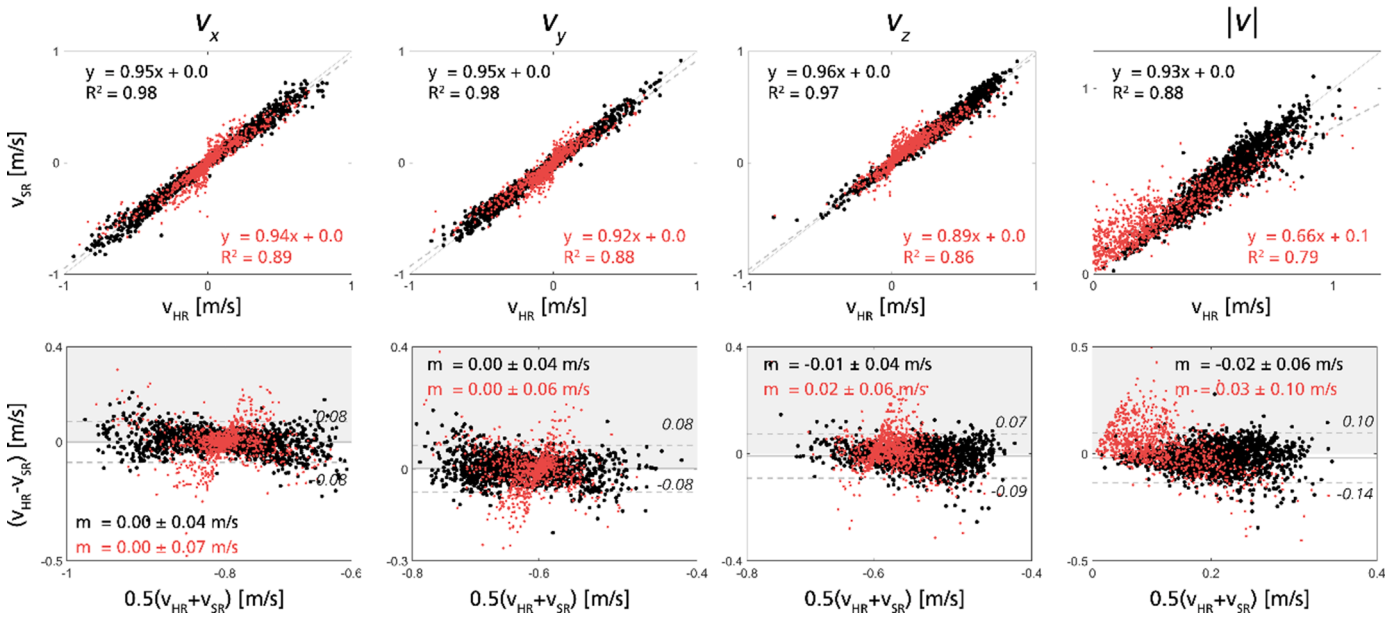

Fig. D.2. Top: Regression plot for each of the velocity components (Vx, Vy, and Vz) and velocity magnitude between ground truth and super-resolved image during the peak flow for the in-silico test case (Subject 3b). Bottom: Bland-Altman plot for each of the velocity components during peak flow. The plots show 5% of the data points (randomly selected) within the vessel core (black) and vessel wall (red), respectively. All data was generated using deterministic sinc upsampling.

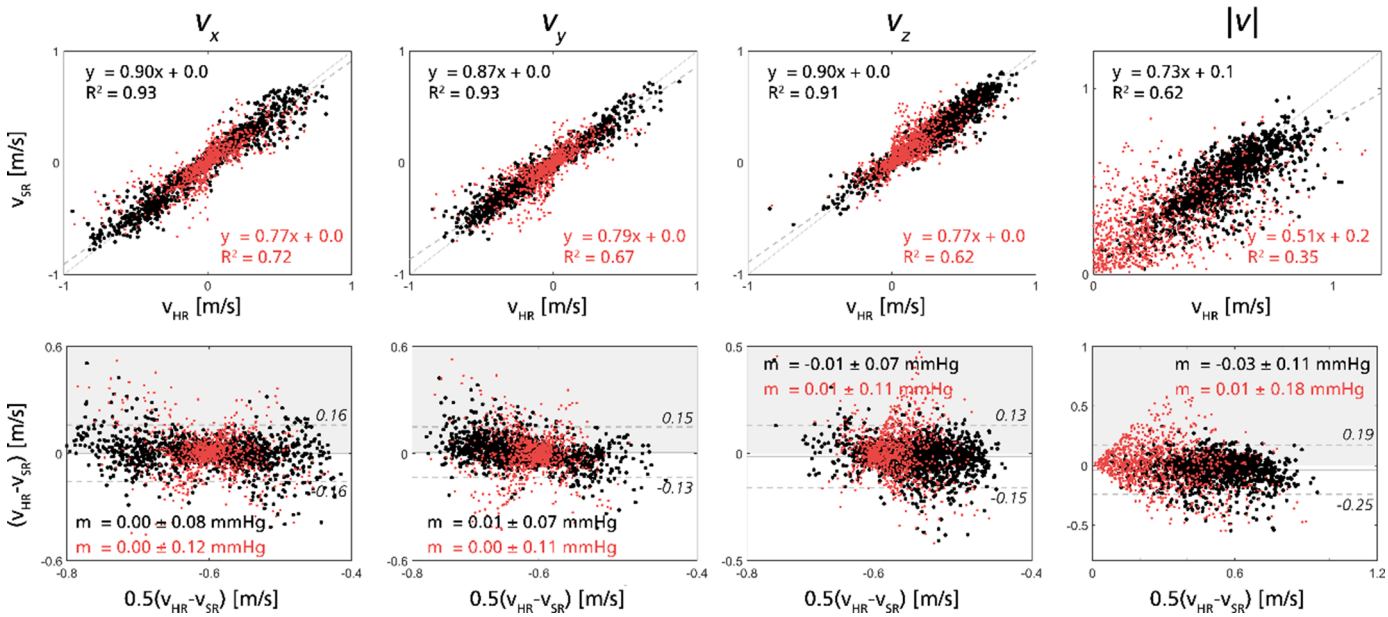

Fig. D.3. Top: Regression plot for each of the velocity components (Vx, Vy, and Vz) and velocity magnitude between ground truth and super-resolved image during the peak flow for the in-silico test case (Subject 3b). Bottom: Bland-Altman plot for each of the velocity components during peak flow. The plots show 5% of the data points (randomly selected) within the vessel core (black) and vessel wall (red), respectively. All data was generated using the original aortic 4DFlowNet.

established biomarker through the challenging cerebrovascular space. Whilst technical differences exist in utilized network design or loss function, and whilst direct head-to-head comparisons are still lacking, the two-step approach presented in our work, and the above-reviewed works, all point to the increasing interest shown in network-driven super-resolution 4D Flow MRI, with the cerebrovascular space being a prime target of where such utilities can have direct clinical impact.

4.6. Limitations

Several limitations are worth pointing out. Firstly, clinical *in-vivo* validation against catheter-based pressure data remains to be performed. Acquiring invasive pressure data in the cerebrovascular space is challenging as intracranial arterial catheterization still awaits regulatory approval in the US. Furthermore, clinical validation of super-resolution utilities is inherently limited in clinical practice. With both 4DFlowNet and the *v*WERP algorithm validated in other domains (Marlevi et al., 2021a, 2019), its potential in improving cerebrovascular quantification is evident. Still, experimental validation in patient-specific *in-vitro* models (as recently attempted in other denoising high-resolution work (Rutkowski et al., 2021)) or in a pre-clinical setting would bring important additional information as to the clinical utility of the presented work.

Secondly, a modest number of *in-silico* models were used for training,

where additional data could enhance network versatility. In particular, including subjects exhibiting significant stenoses *within* the proximal cerebrovascular ROI could add important hemodynamic variations for the utilized training sets, although such models would have to be constructed, validated, and incorporated, in future separate work. Similarly, combining the original aortic and cerebrovascular datasets could generate a more general-purpose utility, although the performance of such would have to be evaluated separately.

Thirdly, it is worth noting that the training of the super-resolution network also depends on the accuracy of the utilized CFD models to capture realistic cerebral flow and pressure. Realistic CFD modeling of cerebral flow is generally challenging due to difficulties in assigning patient-specific boundary conditions. In this work, however, we overcame these challenges by using a previously presented CFD calibration strategy based on cerebral perfusion (non-selective ALS) and flow (PC-MRI) data (Schollenberger et al., 2021). Specifically, the utilized CFD models were validated by comparing the blood supply in the CoW against territorial perfusion data from vessel-selective ALS, where observed high correlations underline the accuracy and applicability of the utilized models.

Fourthly, it should be noted that the utilized network was trained using a range of hyperparameters (patch size, learning rate, batch size, loss function regularization weight, etc.) whos optimal values could still be further optimized. For most of these, set values were chosen empirically from preliminary testing, or simply kept constant from previous training rounds (Ferdian et al., 2020). Moreover, newer network architectures (attention, transformer, graph networks, etc.) may provide further improvements. Still, the satisfactory performance observed for both velocity and relative pressure speaks to the validity of our settings, even if continued systematic fine-tuning could add incremental value. Our work thus provides a fundamental basis for learning super-resolution flow data using synthetic data, alone.

Lastly, practical limitations exist in the increasing data storage required by the super-resolution conversion. Due to the uniformly sampled data representation, a two-fold resolution increase leads to an eight-fold increase in disk space usage. Moreover, the data representation of 4D Flow MRI (e.g., one image cube per velocity component) further complicates the problem. A more flexible data representation, such as adaptable grid representations or graph-based networks (Sanchez-Gonzalez et al., 2020) may offer improved future possibilities circumventing this issue and may be explored in future work.

4.7. Clinical outlook and future work

The expansion of quantitative hemodynamic imaging for cerebrovascular applications promises improved clinical abilities (Leng et al., 2014; Penn et al., 2011; Rivera-Rivera et al., 2018), and the usage of super-resolution 4D Flow MRI presents an effective way of quantifying such hemodynamic markers in the brain, with our work highlighting its accurate recovery of both direct and functional hemodynamic metrics. Importantly, super-resolution imaging circumvents intrinsic obstacles otherwise related to non-invasive cerebrovascular flow quantification (limited spatial coverage; challenging vascular anatomies; etc.), and its clinical potential is therefore particularly evident within this vascular domain.

Numerous, future directions can be envisioned to extend and clarify the capabilities highlighted in our study: additional training data expanding network capabilities, modified architecture improving predictions in near-wall regions, or extended clinical validation against acquired 4D Flow MRI or experimentally derived invasive catheter data. Clinically oriented studies evaluating the potential of super-resolution imaging to improve clinical risk stratification by means of improved relative pressure estimations could also be envisioned in the future. Nevertheless, our data highlights the potential of super-resolution 4D Flow MRI and coupled physics-informed image analysis in the cerebrovascular space.

5. Conclusions

In this study, we have shown how dedicated super-resolution 4D Flow MRI and physics-informed image analysis can in sequence be effectively used to accurately quantify cerebrovascular hemodynamics, including regional velocities, flows, and functional relative pressures. Using dedicated patient-specific *in-silico* data, we have shown how the existing 4DFlowNet network can be effectively repurposed into the cerebrovascular space, successfully converting low-resolution input data into high-resolution equivalents with maintained precision and effective noise-reduction. Furthermore, in sequential combination with the physics-informed deterministic image analysis algorithm *v*WERP, we have shown how conversion into super-resolution data successfully reduces estimation biases in functional relative pressures otherwise observed in the utilized low-resolution input data. Lastly, implementation in an exemplary *in-vivo* cohort shows how improvements in velocity-to-noise-ratio, preserved flow, and converging relative pressures estimates are achievable in a clinical setting.

Ethical approval

For all clinical patient data, acquisitions and study protocols followed institutional review board (IRB) approval and complete informed consent.

Authorship contribution statement

All authors: critical analysis, review, and approval of the final manuscript. E.F. and D.M.: conception of the study, manuscript drafting, method design and implementation, data analysis and interpretation. D. N. and A.A.Y: conception and supervision of the study. J.S.: CFD model preparation and simulations. M.A. and S.S: data acquisition and analysis. C.A.F. and E.R.E.: supervision and manuscript review.

Declaration of Competing Interest

The Authors declare that there is no conflict of interest

Data availability

Data will be made available on request.

Funding

E. F. holds a New Zealand Heart Foundation Scholarship, Grant No. 1786.

D.M. holds a Knut and Alice Wallenberg Foundation scholarship for postdoctoral studies at Massachusetts Institute of Technology.

J.S. is supported by a University of Michigan Rackham Predoctoral Fellowship.

M.A. was supported by a Ruth L. Kirschstein National Research Service Award (NIH F30 HL140910) and the Northwestern – Medical Science Training Program (NIH T32 GM815229).

E.R.E. was funded in part by NIH R01 49039.

A.A.Y. acknowledges core funding from the Wellcome/EPSRC Centre for Medical Engineering (WT203148/Z/16/Z) and the London Medical Imaging and AI Centre for Value-Based Healthcare.

D.N. would like to acknowledge funding from the Engineering and Physical Science Research Council (EP/N011554 and EP/R003866/1).

Appendices

A. Network architecture

The deep residual network structure utilized in this paper is depicted

in Fig. A.1. In principle, this is substantially the same architecture as the previously published 4DFlowNet for large aortic flows (Ferdian et al., 2020). Key differences are highlighted in Section 2.1.1, but to re-iterate, key points include:

1. Patch input size was changed to a 12-voxel cube.
2. Linear output layers were utilized
3. Gradient terms were removed from the loss function.

Note that training setup, hyperparameters, and trained weights are all publicly available at https://github.com/EdwardFerdian/4DFlowNet).

B. Validation of super-resolution performance over additional resolution sets

Corroborating the results in Section 3.1.1 and 3.1.2 similar analysis was performed over a second set of *in-silico* resolutions converting input data at dx = 0.75 mm to super-resolution data at dx = 0.375 mm (comparing against reference high-resolution data sampled directly from the equivalent CFD solution).

B.1. Estimation of super-resolution velocity

As shown in Fig. B.1 and in agreement with the results provided across the 1 mm/0.5 mm resolution pair in the main manuscript, excellent correlations are observed between super-resolution and high-resolution data over all velocity components. Consistently, linear regression slopes and correlation coefficients are $k>0.91$ and $R^2>0.96$ for the vessel core region, and $k>0.95$ and R2>0.74 for the vessel wall region. The Bland-Altman output also indicates no bias shifts introduced by the super-resolved data, with deviations of <0.05 m/s with limits of agreements <0.15 m/s across all components and regions. Regarding the distinction between SR and HR data, only the out-of-plane direction indicate statistically significant differences ($p>0.24$ for v_x and v_y; $p < 0.03$ for v_z). Isolating peak velocity magnitudes, measures in both vessel core (MAE = 0.07 ± 0.06 m/s, relative error = 14.38 ± 0.06%, cosine similarity 0.99 ± 0.06) and vessel wall regions (MAE = 0.12 ± 0.11 m/s and cosine similarity 0.94 ± 0.11) similar with the 0.5/1.0 mm counterpart.

B.2. Estimation of super-resolution relative pressure

Furthermore, Fig. B.2 shows how conversion into super-resolution data mitigates underestimation in relative pressures, with a linear regression slope of changing from $k = 0.83$ at low resolution to $k = 0.98$ at super-resolution (to be compared with $k = 1.02$ at reference high-resolution). Bland-Altman assessments also supplement this same data, where the spread in estimates is reduced with super-resolution, albeit with a slightly remaining underestimation bias (mean shift of −0.25 ± 0.57 mmHg at low resolution; mean shift of −0.24 ± 0.24 mmHg at super-resolution; mean shift of 0.08 ± 0.17 mmHg at reference high resolution; the difference between SR vs. HR remaining statistically significant at $p = 0.002$).

C. Example of super-resolution relative pressure traces

Complementing Section 3.1.2, Fig. C.1 shows example output traces for the right ICA-MCA sections of all four models, respectively. As seen, conversion to super-resolution data mitigates the underestimation bias otherwise observed in the low-resolution input data.

D. Comparative performance of 4DFlowNet and alternative super-resolution approaches

D.1. Estimation of super-resolution velocity

With primary results provided in Section 3.1. of the main manuscript, Figs. D.1–D.3 present linear regression plots and coupled Bland-Altman representations for super-resolved cerebrovascular velocities using bilinear interpolation, sinc interpolation, and the *original* aortic 4DFlowNet, respectively. As described briefly in Section 3.1.3, the determinist bilinear interpolation renders the highest deviation from ground truth data across all velocity components, with a linear regression of in average $k = 0.79$ (vessel core) or $k = 0.62$ (vessel wall). Statistical differences between bilinear interpolation and HR reference velocities can also be inferred for some vessel core entries ($p < 0.001$ for both v_x and v_{mag}).

The same goes for the original aortic 4DFlowNet, with a linear regression of about $k = 0.88$ (vessel core) or $k = 0.78$ (vessel wall); again lower than the re-trained equivalent and with statistical differences inferred against reference HR data for the velocity magnitude entries ($p<0.004$ for both core and wall v_{mag}). Neither bilinear interpolation nor the aortic 4DFlowNet are however associated with any large-scale estimation bias when it comes to super-resolved velocities (mean bias shift = −0.04 ± 0.10 mmHg (vessel core) and 0.0 ± 0.12 mmHg (vessel wall) for bilinear interpolation; −0.03 ± 0.11 mmHg (vessel core) and 0.01 ± 0.18 mmHg (vessel wall) for aortic 4DFlowNet, respectively). Echoing primary results reported in the main manuscript, increasing deviation are also evident with regard to peak velocity in both vessel core and vessel wall regions for both alternative approaches (for bilinear interpolation, vessel core: MAE = 0.12 ± 0.09 m/s, relative error = 33.7 ± 60.9%, cosine similarity = 0.99 ± 0.10, vessel wall: MAE = 0.14 ± 0.11 m/s, cosine similarity = 0.95 ± 0.11. For aortic 4DFlowNet, vessel core: MAE = 0.11 ± 0.08 m/s, relative error = 16.0 ± 19.9%, cosine similarity = 0.99 ± 0.08; vessel wall: MAE = 0.15 ± 0.11 m/s, cosine similarity = 0.93 ± 0.11).

On the contrary, super-resolution utilizing sinc interpolation shows comparatively accurate velocity recovery, with results non-inferior to the cerebrovascular 4DFlowNet approach. Across all velocity components, linear regression is given at an average $k = 0.95$ (vessel core) or $k = 0.85$ (vessel wall), and no dominant estimation bias is observed against high resolution reference (mean bias shift = −0.01 ± 0.04 mmHg (vessel core) and 0.01 ± 0.07 mmHg (vessel wall)). No statistical difference can be inferred against HR reference data in the vessel core ($p>0.20$ across all velocity components), however, deviations are inferred in the out-of-plane direction of the vessel wall component ($p>0.79$ for v_x and v_y; $p = 0.002$ for v_z). These results are also underlined by the errors at peak velocity (vessel core: MAE = 0.06 ± 0.04 m/s, relative error = 22.6 ± 83.9%, cosine similarity = 1.00 ± 0.05, vessel wall: MAE = 0.09 ± 0.07 m/s, cosine similarity = 0.97 ± 0.08).

D.2. Estimation of super-resolution relative pressure

Coupling to *D.1* above and Fig. 6 in the main manuscript, recovery of relative pressures was also derived using the alternative approaches for super-resolution imaging. As described in Section 3.1.3, higher deviations are reported from ground truth high-resolution data across all alternative approaches: bilinear interpolation ($k = 0.66$, $R^2 = 0.99$), sinc interpolation ($k = 0.87$, $R^2 = 1.00$), and aortic 4DFlowNet ($k = 0.87$, $R^2 = 0.99$). Also, in contrast to the re-trained network (see Section 3.1.2), the alternative approaches are all associated with persistent relative pressure estimation bias (mean bias shift = −0.82 ± 1.13, −0.31 ± 0.48, and −0.41 ± 0.58 mmHg for super-resolved data using bilinear interpolation, sinc interpolation, and aortic 4DFlowNet, respectively; with results being significantly inferred for bilinear interpolation and the aortic network). Lastly echoing the data in the main manuscript, peak relative pressure estimates are given at a relative error of 25.0 ± 7.3%, 9.6 ± 5.6%, and 14.8 ± 11.9%, and a MAE of 0.9 ± 1.0 mmHg, 0.3 ± 0.4 mmHg, and 0.4 ± 0.5 mmHg for bilinear interpolation, sinc interpolation, and aortic 4DFlowNet, respectively.

References

Abadi, M., Barham, P., Chen, J., Chen, Z., Davis, A., Dean, J., Devin, M., Ghemawat, S., Irving, G., Isard, M., 2016. Tensorflow: a system for large-scale machine learning. In:

12th {USENIX} symposium on operating systems design and implementation, pp. 265–283 {OSDI} 16.
Aristova, M., Vali, A., Ansari, S.A., Shaibani, A., Alden, T.D., Hurley, M.C., Jahromi, B.S., Potts, M.B., Markl, M., Schnell, S., 2019. Standardized evaluation of cerebral arteriovenous malformations using flow distribution network graphs and dual-venc 4D flow MRI. J. Magn. Reson. Imaging 50, 1718–1730.
Arthurs, C.J., Khlebnikov, R., Melville, A., Marčan, M., Gomez, A., Dillon-Murphy, D., Cuomo, F., Silva Vieira, M., Schollenberger, J., Lynch, S.R., 2021. CRIMSON: an open-source software framework for cardiovascular integrated modelling and simulation. PLoS Comput. Biol. 17, e1008881.
Bratt, A., Kim, J., Pollie, M., Beecy, A.N., Tehrani, N.H., Codella, N., Perez-Johnston, R., Palumbo, M.C., Alakbarli, J., Colizza, W., 2019. Machine learning derived segmentation of phase velocity encoded cardiovascular magnetic resonance for fully automated aortic flow quantification. J. Cardiovasc. Magn. Reson. 21, 1–11.
Fathi, M.F., Perez-Raya, I., Baghaie, A., Berg, P., Janiga, G., Arzani, A., D'Souza, R.M., 2020. Super-resolution and denoising of 4D-Flow MRI using physics-Informed deep neural nets. Comput. Methods Programs Biomed. 197, 105729.
Ferdian, E., Suinesiaputra, A., Dubowitz, D.J., Zhao, D., Wang, A., Cowan, B., Young, A. A., 2020. 4DFlowNet: super-resolution 4D Flow MRI using deep learning and computational fluid dynamics. Front Phys 8, 138.
Gottwald, L., Töger, J., Bloch, K.M., Peper, E., Coolen, B., Strijkers, G., van Ooij, P., Nederveen, A., 2020. High Spatiotemporal Resolution 4D Flow MRI of Intracranial Aneurysms at 7T in 10 Min. Am. J. Neuroradiol. 41, 1201–1208.
Han, Y.F., Liu, W.H., Chen, X.L., Xiong, Y.Y., Yin, Q., Xu, G.L., Zhu, W.S., Zhang, R.L., Ma, M.M., Li, M., 2016. Severity assessment of intracranial large artery stenosis by pressure gradient measurements: a feasibility study. Catheter. Cardiovasc. Interv. 88, 255–261.
Kissas, G., Yang, Y., Hwuang, E., Witschey, W.R., Detre, J.A., Perdikaris, P., 2020. Machine learning in cardiovascular flows modeling: predicting arterial blood pressure from non-invasive 4D flow MRI data using physics-informed neural networks. Comput. Method. Appl. Mech. Eng. 358, 112623.
Lamata, P., Pitcher, A., Krittian, S., Nordsletten, D., Bissell, M.M., Cassar, T., Barker, A.J., Markl, M., Neubauer, S., Smith, N.P., 2014. Aortic relative pressure components derived from four-dimensional flow cardiovascular magnetic resonance. Magn. Reson. Med. 72, 1162–1169.
Leng, X., Wong, K.S., Liebeskind, D.S., 2014. Evaluating intracranial atherosclerosis rather than intracranial stenosis. Stroke 45, 645–651.
Marlevi, D., Balmus, M., Hessenthaler, A., Viola, F., Fovargue, D., de Vecchi, A., Lamata, P., Burris, N.S., Pagani, F.D., Engvall, J., 2021a. Non-invasive estimation of relative pressure for intracardiac flows using virtual work-energy. Med. Image Anal. 68, 101948.
Marlevi, D., Ruijsink, B., Balmus, M., Dillon-Murphy, D., Fovargue, D., Pushparajah, K., Bertoglio, C., Colarieti-Tosti, M., Larsson, M., Lamata, P., Figueroa, C.A., Razavi, R., Nordsletten, D., 2019. Estimation of cardiovascular relative pressure using virtual work-energy. Sci. Rep. 9, 1375.
Marlevi, D., Schollenberger, J., Aristova, M., Ferdian, E., Ma, Y., Young, A.A., Edelman, E.R., Schnell, S., Figueroa, C.A., Nordsletten, D., 2021b. Non-invasive quantification of cerebrovascular pressure changes using 4D Flow MRI. in-press.
Metcalf, M., Xu, D., Okuda, D.T., Carvajal, L., Srinivasan, R., Kelley, D.A., Mukherjee, P., Nelson, S.J., Vigneron, D.B., Pelletier, D., 2010. High-resolution phased-array MRI of the human brain at 7 tesla: initial experience in multiple sclerosis patients. J. Neuroimaging 20, 141–147.
Morgan, A.G., Thrippleton, M.J., Wardlaw, J.M., Marshall, I., 2021. 4D flow MRI for non-invasive measurement of blood flow in the brain: a systematic review. J. Cereb. Blood Flow Metab. 41, 206–218.
Nath, R., Callahan, S., Singam, N., Stoddard, M., Amini, A.A., 2020. Accelerated phase contrast magnetic resonance imaging via deep learning. In: 2020 IEEE 17th International Symposium on Biomedical Imaging (ISBI). IEEE, pp. 834–838.
Oksuz, I., Clough, J., Bustin, A., Cruz, G., Prieto, C., Botnar, R., Rueckert, D., Schnabel, J. A., King, A.P., 2018. Cardiac MR Motion Artefact Correction from K-Space Using Deep Learning-Based reconstruction, International Workshop On Machine Learning For Medical Image Reconstruction. Springer, pp. 21–29.
Penn, D.L., Komotar, R.J., Connolly, E.S., 2011. Hemodynamic mechanisms underlying cerebral aneurysm pathogenesis. J. Clin. Neurosci. 18, 1435–1438.
Perez-Raya, I., Fathi, M.F., Baghaie, A., Sacho, R.H., Koch, K.M., D'Souza, R.M., 2020. Towards multi-modal data fusion for super-resolution and denoising of 4D-Flow MRI. Int J Numer Method Biomed Eng 36, e3381.
Plenge, E., Poot, D.H., Bernsen, M., Kotek, G., Houston, G., Wielopolski, P., van der Weerd, L., Niessen, W.J., Meijering, E., 2012. Super-resolution methods in MRI: can they improve the trade-off between resolution, signal-to-noise ratio, and acquisition time? Magn. Reson. Med. 68, 1983–1993.
Rivera-Rivera, L., Johnson, K., Turski, P., Wieben, O., 2018. Pressure Mapping and Hemodynamic Assessment of Intracranial Dural Sinuses and Dural Arteriovenous Fistulas with 4D Flow MRI. American Journal of Neuroradiology.
Rutkowski, D.R., Roldán-Alzate, A., Johnson, K.M., 2021. Enhancement of cerebrovascular 4D flow MRI velocity fields using machine learning and computational fluid dynamics simulation data. Sci. Rep. 11, 1–11.
Sanchez-Gonzalez, A., Godwin, J., Pfaff, T., Ying, R., Leskovec, J., Battaglia, P., 2020. Learning to simulate complex physics with graph networks. In: International Conference on Machine Learning. PMLR, pp. 8459–8468.
Schnell, S., Ansari, S.A., Wu, C., Garcia, J., Murphy, I.G., Rahman, O.A., Rahsepar, A.A., Aristova, M., Collins, J.D., Carr, J.C., 2017. Accelerated dual-venc 4D flow MRI for neurovascular applications. J. Magn. Reson. Imaging 46, 102–114.
Schollenberger, J., Figueroa, C.A., Nielsen, J.F., Hernandez-Garcia, L., 2020. Practical considerations for territorial perfusion mapping in the cerebral circulation using super-selective pseudo-continuous arterial spin labeling. Magn. Reson. Med. 83, 492–504.
Schollenberger, J., Osborne, N.H., Hernandez-Garcia, L., Figueroa, C.A., 2021. A combined computational fluid dynamics and MRI Arterial Spin Labeling modeling strategy to quantify patient-specific cerebral hemodynamics in cerebrovascular occlusive disease. Front. Bioeng. Biotechnol. 689.
Shit, S., Das, D., Ezhov, I., Paetzold, J.C., Sanches, A.F., Thuerey, N., Menze, B.H., 2021. In: Velocity-To-Pressure (V2P)-Net: Inferring Relative Pressures from Time-Varying 3D Fluid Flow Velocities, International Conference on Information Processing in Medical Imaging. Springer, pp. 545–558.
Stankovic, Z., Allen, B.D., Garcia, J., Jarvis, K.B., Markl, M., 2014. 4D flow imaging with MRI. Cardiovasc. Diagn. Ther. 4, 173–192.
Vali, A., Aristova, M., Vakil, P., Abdalla, R., Prabhakaran, S., Markl, M., Ansari, S.A., Schnell, S., 2019. Semi-automated analysis of 4D flow MRI to assess the hemodynamic impact of intracranial atherosclerotic disease. Magn. Reson. Med. 82, 749–762.
Van Reeth, E., Tham, I.W., Tan, C.H., Poh, C.L., 2012. Super-resolution in magnetic resonance imaging: a review. Concept. Magnet. Resonan. Part A 40, 306–325.
Wang, H., Yang, Z., Li, B., Wang, S., 2020. Predicting the near-wall velocity of wall turbulence using a neural network for particle image velocimetry. Phys. Fluid. 32, 115105.